LUND UNIVERSITY

A numerical study on orientational arrest and size segregation of dense particle flows using discrete element modeling

Yousefian, Zakiyeh

2023

Document Version:
Publisher's PDF, also known as Version of record

[Link to publication](#)

Citation for published version (APA):
Yousefian, Z. (2023). *A numerical study on orientational arrest and size segregation of dense particle flows using discrete element modeling*. Lund University (Media-Tryck).

Total number of authors:
1

A numerical study on orientational arrest and size segregation of dense particle flows using discrete element modeling

ZAKIYEH YOUSEFIAN
DIVISION OF COMPUTATIONAL CHEMISTRY | FACULTY OF SCIENCE | LUND UNIVERSITY

A numerical study on orientational arrest and size segregation of dense particle flows using discrete element modeling

A numerical study on orientational arrest and size segregation of dense particle flows using discrete element modeling

by Zakiyeh Yousefian

LUND
UNIVERSITY

Thesis for the degree of Licentiate
Thesis advisors: Prof. Martin Trulsson
Faculty opponent: Prof. Johan Revstedt

To be presented, with the permission of Lund University on Friday, the 26th of January 2024 at 9:30.

Organization **LUND UNIVERSITY**	Document name **LICENTIATE THESIS**	
Department of Chemistry Box 124 SE–221 00 LUND Sweden	Date of disputation 2024-01-26	
	Sponsoring organization	
Author(s) Zakiyeh Yousefian		
Title and subtitle A numerical study on orientational arrest and size segregation of dense particle flows using discrete element modeling		

Abstract

The thesis focuses on studying dense particle flows, which are either dry or submerged in a Newtonian fluid through two dimensional numerical simulations using the discrete element method (DEM). The First paper deals with dense suspensions in viscous regime under oscillatory planar shear. We found that having an oscillatory shear can help reducing the viscosity of the suspension. Also, in the frictional case oscillation can increase the suspension's shear jamming packing fraction. Furthermore, at small oscillatory strains, frictionless ellipses become dynamically arrested in their initial orientational configuration.

In the second paper, we studied size segregation in a bi-disperse mixture of big and small discs. We applied an iterative force measurement technique to find the restoring/segregation force on big and small particles in the system when we have constant or linearly increasing vertical gravity. Our method works equivalently well as a previously introduced method for the case of having a constant vertical gravitational field while it can find the restoring force for the case of linearly increasing gravity whereas the other method fails to measure the force.

DOKUMENTDATABLAD enl SIS 61 41 21

Key words granular flow, dense suspensions, oscillatory shear rheology, segregation, elliptical particle flow, discrete element method		
Classification system and/or index terms (if any)		
Supplementary bibliographical information	Language English	
ISSN and key title	ISBN 978-91-7422-964-6 (print) 978-91-7422-965-3 (pdf)	
Recipient's notes	Number of pages 122	Price
	Security classification	

Signature _____   Date ____2023-12-19_____

A numerical study on orientational arrest and size segregation of dense particle flows using discrete element modeling

by Zakiyeh Yousefian

LUND
UNIVERSITY

A licentiate thesis at a university in Sweden takes either the form of a single, cohesive research study (monograph) or a summary of research papers (compilation thesis), which the licentiate student has written alone or together with one or several other author(s).

In the latter case the thesis consists of two parts. An introductory text puts the research work into context and summarizes the main points of the papers. Then, the research publications themselves are reproduced, together with a description of the individual contributions of the authors. The research papers may either have been already published or are manuscripts at various stages (in press, submitted, or in draft).

Cover illustration front: Zakiyeh Yousefian

To my beloved parents and kids

Contents

List of publications

This thesis is based on the following publications, referred to by their Roman numerals:

I   **Orientational arrest in dense suspensions of elliptical particles under oscillatory shear flows**
Z. Yousefian, M. Trulsson
Europhysics Letters, 2022, 136(3), pp. 36002

II   **An iterative method for measuring spatial segregation forces in bi-disperse granular flow mixtures under various gravity fields**
Z. Yousefian, M. Trulsson
To be submitted to JFM

All papers are reproduced with permission of their respective publishers.

Acknowledgements

I would like to first thank my supervisor Martin Trulsson. Thanks for always being supportive, helpful and so patient to me. Thanks for giving me the opportunity to join your group and learn a lot. It's really a nice experience for me to work with you.

I would also like to thank the former PhD student Junhao Dong. You are always willing to help. Thanks for answering my questions every now and then.

I would like to thank the post-doc in our group Pappu Acharya and also my office mate Iria Bolano for always being so nice and helpful.

I thank everyone in the division of Computational Chemistry and Physical Chemistry. I enjoy this fun and friendly working environment.

Thanks to my lovely kids for always bringing me happiness and motivation. Thanks to my beloved parents and brother for supporting me.

Popular summary in English

When we use the term ¨granular material¨ we are not talking about a single particle, but rather piles of solid particles that can be either dry, wetted as in sand-castles (with liquid bridges), or immersed in a fluid, with the latter called suspensions. There are many examples of granular materials everywhere from corn starch and flour in our kitchen to wet cement and cement powder used in building resilient structures, to debris flows known as a common natural hazard. So, it is important to have a deeper understanding of the physics of granular materials both to be able to predict their behavior and to produce materials of desired properties.
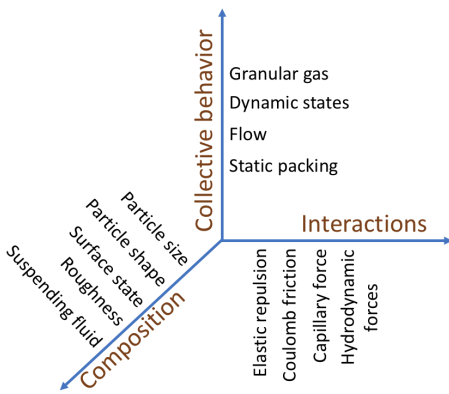
Granular material is a collection of different types of materials that can be very diverse considering particle properties, interactions, and process dynamics. While particle properties and interactions can define what kind of material we are dealing with, process dynamics can show different states of packing depending on the boundary conditions, energy input, etc. Models to study granular materials are generally based on the simplest types of materials as reference cases, for instance, a continuous steady flow of isotropic particles (i.e. discs or spheres) of nearly the same size, only interacting through elastic repulsion and friction.

These simple models help us understand the simplest particle flows, a small subset of all granular systems. Nevertheless, they serve as a good reference case, allowing us to disentangle the effect of other parameters, like shape anisotropy, polydispersity in size, different suspending fluids, etc. Furthermore, some phenomena are case-specific and are not observed in simple configurations. Therefore, to improve our understanding of more realistic flows we here study the rheology (the science of measurement of deformation and flow of matter) of packings consisting of elliptical particles with a focus on the effect of the shape anisotropy on the mechanical response of the system. We also study a common complex phenomenon in granular flows referred to as segregation. Any small differences in particle properties such as size, shape, density, friction, etc can lead to flow-induced segregation. Here, we investigated size segregation in mixtures of big and small discs.

A numerical study on orientational arrest and size segregation of dense particle flows using discrete element modeling

Chapter 1

Introduction

Granular materials are conglomerations of discrete solid particles larger than the atomic scale in a sense that their surfaces are well defined and distinct from their volumes, and that thermal agitation can be ignored. At ambient conditions this corresponds to lower size limit of 1 µm. Particles below this limit is instead referred to as colloids.

Such materials can either be dry or suspended in a viscous liquid, with the latter being called wet granular materials or suspensions. Granular materials are ubiquitous, from natural processes to various industries. We can find examples of them in daily home products (paint, tooth paste, cornstarch), biological systems (blood), industrial processing (waste slurries), construction materials (cement), and geological processes (land sliding). They are a class of complex fluids that can be further categorised based on the physical and chemical properties of the suspended particles and the suspending fluid. Such systems have emerged as an important field of study not only due to their rich physics but also because of their various practical applications [1, 2, 3].

For a single solid particle, Newton's second law can well describe the particle's motion or in the case of two solid particles in contact or a particle immersed in a fluid, there are several theories available to describe the forces. However, when it comes to granular materials, these apparently simple systems, not all of their features can be predicted by available physics theories, such as Newton's second law. So, their behaviour still resists basic understanding and raises many open questions *e.g.* existence of a consolidated constitutive law, and what can gives rise to it, *i.e.* how microscopic parameters and fluctuations lead to a certain rheological behaviour is still an unsettled challenge.

In the present work, I studied numerically both dry and wet granular flows utilizing discrete element method (DEM), where the particles are described individually. For the dense suspensions the fluid is considered as a continuum. I specifically focus both

on the effect of the shape an-isotropy of the particles (compared to the isotropic case) on the system's rheology in oscillatory shear flows, and also on the phenomena that can result from differences in particles' sizes *e.g.*, segregation. I study two dimensional particles that are rigid discs with and without friction. Particles are non-Brownian (*i.e.* the particles have large enough radius for thermal fluctuations to be neglected), repulsive. In the case of dense suspensions the particles are also neutrally buoyant (*i.e.* having the same density as the fluid, so no creaming/sedimentation in the suspension). The suspending fluid in case of a suspension is Newtonian *i.e.* shear stresses depends linearly on the shear-rates/deformation-rates.

Chapter 2

Theory

While the behavior of a single grain is governed by the laws of mechanics, which have not changed much since Coulomb and Newton, the collective physics of a sand pile still resists our understanding. Dealing with granular materials, we encounter many difficulties among which we can mention: 1) Large number of particles in granular media which makes it challenging to simulate the system even with present computer power. 2) Granular materials being athermal, since the particles in a granular medium are too large to have Brownian motion, applying statistical thermodynamics on the system is a bit problematic (due to the lack of temperature). Even though a granular temperature and an Edwards ensemble can be defined. 3) Lack of a clear scale separation between the microscopic scale, *i.e.* the grain size and the macroscopic scale, *i.e.* the size of the flow to have a well-founded continuum description of the system. 4) Complex grain-grain and grain-fluid interactions. 5) Dissipation (inelastic collisions, frictional dissipation) at the microscopic level, which makes it not possible to apply the classical concepts developed in statistical mechanics to granular materials. 6) Different states of matter (such as solid, liquid, and gas) are possible for granular materials, which differ very significantly from those of their molecular counterparts. Among other things, practically all states of granular matter are metastable. Clearly, the root cause of these and other properties peculiar to granular matter is the dissipative nature of the particle interactions.

2.1   Interactions at the particle scale

The contact force between two dry granules is usually divided into a normal and a tangential part. The dominating macroscopic laws of the contact forces are elastic

repulsion (Hertz or harmonic contact) and solid friction (Coulomb's law). There might sometimes also be inelastic normal forces needed for dry grains, as otherwise, we would heat the system, where we have a viscous damping at contact (leading to a coefficient of restitution). In many problems when there is also a suspending fluid present in the system, hydrodynamic forces need to be taken into account as well. There would also be the Buoyancy/Archimedes force, which is the force resulting from the stress that would be exerted on the particle as if the latter had the density of the fluid. Another existing force in the case of having an interstitial fluid, is the *Lubrication force*. Establishing a contact between the grains, needs that the fluid be drained out across quite narrow fluid films. These strong gradient flows lead to hydrodynamic forces called lubrication [4]. A detailed expression of the forces comes in the following chapter.

2.2   Granular packing, jamming, RCP and RLP

Packings of particles are initially identified by a property called packing fraction, which is described as the ratio between the volume occupied by the particles and the total volume occupied by the packing [4]:

$$\phi = \frac{V_{\text{particles}}}{V_{\text{total}}} \tag{2.1}$$

while packings of simple objects like squares, rectangles, cubes, etc, are space-filling, packings of monodisperse discs or spheres will always have voids. There exist a range of packing fractions, from a loosest to a densest, where we find stable packings of such particles. Generally the volume fraction lies between these minimum and maximum values. Maximum packing fraction for monodisperse discs is ~ 0.9069 and is ~ 0.7405 for spheres of equal size [5]. Considering more realistic packings with non iso-tropic particles, one can look at equally sized ellipses (two-dimensional) or ellipsoids (three-dimensional). The densest known packing of ellipses is the same as discs [6], while ellipsoids have been found to pack denser than spheres at packing fraction of ~ 0.7707 [7]. The value was found for aspect ratios equal to or greater $\sqrt{3}$ (prolate ellipsoids) or smaller than $1/\sqrt{3}$ (oblate ellipsoids). Increasing polydispersity leads to amorphous packings rather than crystalline packings. An amorphous configuration is composed of a set of configurations that can (initially) withstand mechanical deformation such as shear [5]. These configurations are denoted *jammed* which are usually represented by their average packing fraction. *Random close packing* (RCP) is the jamming point obtained from isotropic compaction. In case of nearly frictionless

particles, RCP occurs at ~ 0.84 and ~ 0.64 for discs and spheres, respectively, which are both smaller than their corresponding crystalline packing. In the case of polydisperse ellipses and ellipsoids, RCP depends on the aspect ratio [5]. It is also possible to find RCP for monodisperse ellipses and ellipsoids. The value for monodisperse ellipses is ~ 0.895 at aspect ratio of 1.4, the same value as for polydisperse ellipses [8, 9]. For monodisperse ellipsoids, RCP varies in the range $\sim 0.70 - 0.74$ depending on the type of the ellipsoid [10, 11].

Considering frictional particles instead, the jamming points occur at looser packings, referred to as *random loose packing* (RLP) [12]. Corresponding RLP values for frictional discs and spheres are ~ 0.8 and ~ 0.6, respectively. For frictional equally sized ellipses and ellipsoids, there exist similar fashion, however precise values depends on the aspect ratio [9, 13].

If the above systems undergo shearing, they might shear jam. Shear jamming packing fraction usually occurs at packing fractions lower than the corresponding RLP for frictional configurations. Upon shear, anisotropy is induced in the system via anisotropic forces and contact networks. By that, the number of force-bearing particles increases compared to the RCP at the same packing fraction. While for frictionless grains RCP and shear jamming occur at the same packing fraction, for frictional grains the shear-jamming is considerably lower than RLP, leading to a dilatency of a granular packing under shear (wherein the volume of a granular packing increases upon shear deformation)[14, 15, 16]. Recent studies, however, show that dillatancy can happen for frictionless packings as well[17]. I will throughout the thesis look at ϕ.

2.2.1 Number of contacts

Let us consider N hard frictionless identical particles with diameter d at equilibrium, where N_c is the total number of contacts in the configuration and D indicates the dimensions of the system (2 or 3). Since the contacts are frictionless, the inter-particle forces are perpendicular to the plane of contact, so there are N_c unknown forces. In two (three) dimensions, we can write $2N(3N)$ equilibrium equations. Angular-momentum balance is automatically satisfied since all forces are central. Considering the packing is at mechanical equilibrium, there exists at least one solution for the force distribution. So, there needs to be fewer equations than the unknowns $DN \leq N_c$. If we call the average number of contacts per particle $Z = 2N_c/N$, *coordination number*, the above condition implies that $Z \geq 2D$. Remembering that the particles are rigid, the distance between particle i and particle j in contact should be equal to the diameter, *i.e.* $|r_i - r_j| = d$. We will have N_c equations of such kind. To be able to find a solution for these equations, the number of contacts needs to be smaller than the degrees of freedom of the configuration, *i.e.* $N_c \leq DN$ ($Z \leq$

$2D$). So when the frictionless pile is at rest, having both the geometrical constraints and the number of equilibrium equations, leads to $Z = 2D$. Since the number of unknowns and the number of equations are exactly the same, forces are also possible to calculate after the positions are determined. This condition that forces can be calculated without any redundancy is called *isostaticity*, which is a common property of frictionless packings. The story changes drastically when friction is introduced to the system. While the geometrical constraints remain the same as for the frictionless rigid particles ($Z \leq 2D$), the number of force and torque balances changes due to having frictional contacts. In two (three) dimensions there are $2N_c$ ($3N_c$) unknown forces. Mechanical balance gives DN equations for the force balance and $ND(D-1)/2$ for the angular-momentum balance. So, in two (three) dimensions we have $2N_c \geq 3N$ ($3N_c \geq 6N$) and in general we have $DN_c \geq N(D + D(D-1)/2)$. This means that the coordination number should lie in the range $3 \leq Z \leq 4$ ($4 \leq Z \leq 6$) in two (three) dimensions. The general relation would be $D + 1 \leq Z \leq 2D$ [4, 18]. By definition, particles having 2 or more contacts are called non-rattlers. For elliptical particles, the contact plane between two particles is not necessarily perpendicular to the vectors pointing from the center of each ellipse to the contact point [5]. So for elliptical, the angular momentum balance is not satisfied automatically even in the frictionless case since the interparticle forces perpendicular to the contact plane are not central. Adding friction to the system, we will have tangential contact forces as well similar to what happens for discs [5].

2.2.2 Force distribution

As mentioned earlier, despite having a simple definition, granular materials can exhibit considerably different mechanical properties under different external forces and boundary conditions [19]. This behavior is linked to the heterogeneously distributed force chains formed by inter-particle forces [20]. Looking statistically at this heterogeneous force field, we find a typical profile for the probability distribution $P(f)$ of the forces' amplitudes indicated in Fig. 2.1. As observed initially from the figure, the range of force amplitudes is wide. Secondly, we look at the trend of the profile, where we detect a flat zone for forces f bellow the mean force f_0, with $P(f) \propto (f/f_0)^\alpha$ and α very close to zero. On the other hand, for large forces (*i.e.* $f > f_0$), the distribution has an exponential behaviour. $P(f)$ is proportional to $\mathrm{e}^{-\beta f/f_0}$, with β between 1 and 2. Although varying due to statistical reasons and depending on the measuring method, the general shape of the probability distribution for large and small forces is a very robust characteristic for various configurations with or without friction between the particles [4]. Looking at particle elongation (like for elliptical particles) as another effective parameter, one expects that it mainly affect the distribution of weak forces by making the exponential tail of the profile longer. The profile for the probability

distribution of the forces can be described in a more general form of [21, 22]

$$
P(f) = \begin{cases} e^{-\beta(\eta)(f/f_0)}, & f > f_0 \\ (\frac{f}{f_0})^{\alpha(\eta)}, & f < f_0. \end{cases}
\tag{2.2}
$$

where $\eta = \Delta R/R$ is a dimensionless parameter representing the deviation of the particle shape from a circle. $\Delta R = R' - R$ shows the difference between the major radius R' and the minor radius R of the particle. It was found that the force distributions become increasingly broader and more inhomogeneous as particles get more elongated [21]. Hence, the exponential tail of the profile becomes longer for $\eta \neq 0$ and the power law region corresponding to the weak forces changes slope depending on the η parameter.

To be able to characterize the force network, we also need to know the angular distribution of contacts and forces, which are called the *geometrical fabric* and the *mechanical fabric*, respectively. In two dimensions, the geometrical fabric is given by a π-periodic probability density function (since the contacts have no intrinsic polarity, the probability density function is π-periodic rather than 2π-periodic). The function gives the probability of having contact at angle θ, with θ being the angle between the line connecting the centers of two particles in contact and a reference axis depending on the system. Usually, a truncated second-order Fourier expansion is used to describe the geometrical fabric as :

$$
\xi(\theta) \approx \frac{1}{\pi}[1 + A_c \cos 2(\theta - \theta_c)],
\tag{2.3}
$$

where A_c gives the lowest order fabric anisotropy of the material and θ_c is its principal direction [4, 23, 24].

In a similar manner, the mechanical anisotropy of the average normal forces $F_n(\theta)$, denoted as A_n, and the average friction forces $F_t(\theta)$, denoted as A_t, can be obtained from their corresponding Fourier expansion, respectively as:

$$
F_n(\theta) \approx \frac{f_0}{2\pi}[1 + A_n \cos 2(\theta - \theta_f)],
\tag{2.4}
$$

$$
F_t(\theta) \approx \frac{f_0}{2\pi} A_t \sin 2(\theta - \theta_f),
\tag{2.5}
$$
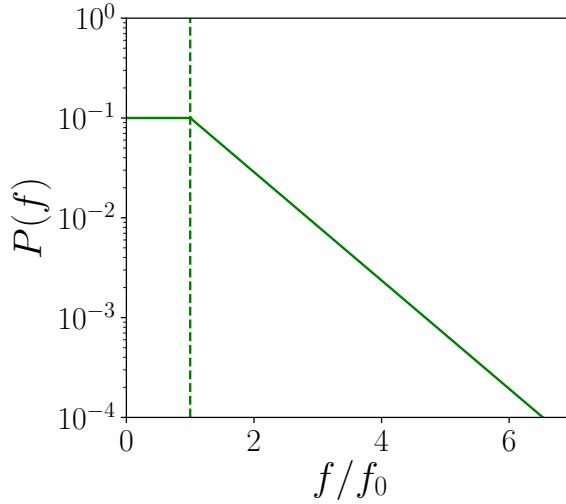
Figure 2.1: A schematic view of the distribution of the force amplitudes. The horizontal axis shows the normalized force values and the vertical axis shows the probabilities. The dashed vertical line indicates where f equals f_0.

It's possible to distinguish between the strong and the weak contact network forces by separately plotting the angular distribution function of forces above and below the mean force f_0. This can be done both for isotropic (such as circles) and anisotropic (such as ellipses) particles. In a more general approach, we consider various geometrical and mechanical fabrics for the ¨ζ networks¨ defined as the subsets of contacts bearing a force below a cutoff normalized value ζ, *i. e.* $0 \leq f/f_0 \leq \zeta$, where ζ can vary from a 0 to the maximum force in the system. Therefore, a continuous family of angular distributions belonging to different ζ networks can be obtained that describes the geometrical and mechanical state of the system [22].

2.3   Granular liquid

While a granular medium can behave like a solid as was discussed earlier, it can also behave similar to a gas in the opposite limit, when subjected to strong external stimuli, like strong shaking in a box. In this gaseous regime, particles interact mainly through binary collisions. Development of the kinetic theories of the granular media that can provide constitutive laws for such diluted particle flows was based on the analogy between agitated granules and molecules in a gas [4]. Most granular flows, however, exist between these two limits of quasi-static and gaseous regimes. Particle interactions in this *liquid* dense regime are both by collisions and long-lived contacts. More details on granular flows in the dense regime come in the following sections.

2.3.1 $\mu(I)$ **rheology**

When we study dense granular flows, we are primarily interested in the constitutive laws and how the material flows under stress. From a phenomenological perspective, granular flows belong to the family of visco-plastic materials, where there exists a flow threshold and afterward, when the material starts to flow, there exists a quadratic shear-rate dependence which resembles a viscous behavior [4].

The rheological properties of such flows can be measured by different rheometers, such as cone plates, parallel plates, and Couette rheometers. While most of the rheometers work at constant volume, introducing a pressure-controlled rheometer recently, was a significant step towards having a continuous description of flowing granular media which has long been a challenge [25].

In a pressure-imposed rheometer, as in Fig. 2.2, the whole assembly of hard particles is sheared at a given shear rate $\dot{\gamma} = 2U/H$ and a confining pressure P. The medium is then free to dilate or to compact with a top plate moving vertically. In the case of a suspension, the top plate is porous allowing the suspending fluid in and out, see Fig. 2.5. Dense suspensions will be discussed in more detail in the next section.

Now considering pressure-imposed shearing of dry granular media or when the inertial forces are dominating compared to viscous effects in a granular suspension, there is only one dimensionless control parameter called *inertial number*,

$$I = \frac{\dot{\gamma}d}{\sqrt{P/\rho_p}} \tag{2.6}$$

with d and ρ_p being the diameter and the density of the particles. This inertial number I, can be interpreted in terms of the ratio between two time scales $I = t_{micro}/t_{macro}$, where $t_{micro} = d/\sqrt{P/\rho}$ is the inertial time of rearrangement and $t_{macro} = 1/\dot{\gamma}$ is the time scale related to the mean shear rate [4, 25]. The granular rheology is characterized by two functions of the inertial number [4]:

$$\tau = \mu(I)P \tag{2.7}$$

$$\phi = \phi(I) \tag{2.8}$$

Fig. 2.3 depicts an illustrative view of $\mu(I)$ and $\phi(I)$ functions. As seen from the figure both μ and ϕ reach plateau values, denoted as μ_c and ϕ_c, respectively, as I approaches zero. μ_c represent the flow threshold and ϕ_c is the jamming packing fraction.
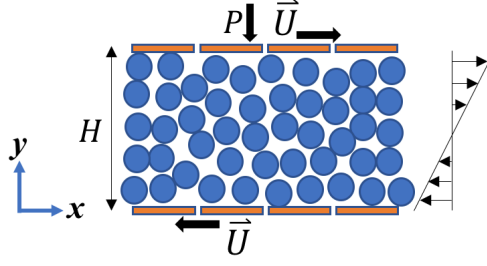
Figure 2.2: Paradigmatic configurations of pressure-imposed shear of dry granular media.

Assuming local rheology, *i.e.*, when the stresses only depend on the local shear rate, $\dot\gamma(y)$, and on the local pressure, $P(y)$, and also considering that particles might be of different sizes and have a diameter distribution $d(y)$ over the slab, we can generalize Eq. 2.7 and 2.8 to describe inhomogeneous shear flows with $I(y) = |\dot\gamma(y)d(y)|/\sqrt{P(y)/\rho_p}$. With this assumption, the rheology can be further generalized to a tensorial form to picture complex three-dimensional flows sheared in different directions. The stress tensor can be written as:

$$\sigma_{ij} = -P\delta_{ij} + \tau_{ij} \tag{2.9}$$

In Eq. 2.15, P is the isotropic pressure, δ_{ij} is the Kronecker delta matrix (further information on how the stresses are measured comes in section 3.4 in the next chapter) and

$$\tau_{ij} = \eta_{\text{eff}}\dot\gamma_{ij} \tag{2.10}$$

with $\eta_{\text{eff}} = \mu(I)P/|\dot\gamma|$ being an effective viscosity, and $|\dot\gamma| = \sqrt{\frac{1}{2}\dot\gamma_{ij}\dot\gamma_{ij}}$ the second invariant of the shear-rate tensor $\dot\gamma_{ij} = \frac{\partial u_i}{\partial x_j} + \frac{\partial u_j}{\partial x_i}$ where u_i is velocity field. Modifying the inertial number according to the specific setup like above, $\mu(I)$ rheology is applicable to some other configurations of particle flows, such as flows of non-circular or polydisperse grains, flows down an inclined plane or flows of size segregated particles as well (like in paper II) [4, 26].

2.3.2 Bagnold's law

If the granular medium is instead sheared at constant volume fraction ϕ (as in traditional approaches to study rheology), by keeping the distance between the two con-
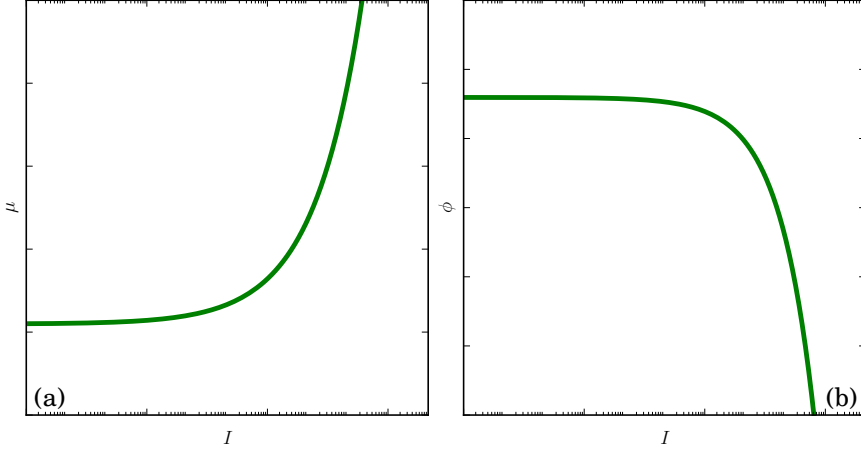
Figure 2.3: Schematic profiles of (a) $\mu(I)$ and (b) $\phi(I)$. The horizontal axis is in log scale.

fining walls in Fig. 2.2 constant, the controlling parameters will be ϕ, $\dot{\gamma}$, d and ρ_p. Using dimensional analysis, the shear stress and the pressure will be written as:

$$\tau = \rho_p d^2 f_1(\phi)\dot{\gamma}^2 \tag{2.11}$$

$$P = \rho_p d^2 f_2(\phi)\dot{\gamma}^2 \tag{2.12}$$

where, f_1 and f_2 are empirical functions of the packing fraction. Eq. 2.11 and 2.12 are called Bagnold's law and are valid for homogenous flows. [27]. For non-homogeneous flows local diameter and shear rate should be in Eq. 2.11 and 2.12.

2.4 Suspensions: immersed granular media

In the previous sections, we discussed dry granular materials. However, in many applications, there exists a suspending fluid in which the particles are immersed. Such systems are referred to as suspensions. Having an interstitial fluid, the interactions between the particles and the continuum fluid phase need also to be accounted for. Although the suspending fluid can be of any nature (shear-thinning, shear-thickening, Bingham, etc), in this study we address incompressible Newtonian fluid, whose motion is governed by *Navier-Stokes* equations, *i.e.* the Eulerian representation of the continuity equation for an incompressible fluid:

$$\nabla . \mathbf{u} = 0 \qquad (2.13)$$

And the conservation of momentum equation:

$$\rho[\frac{\partial \mathbf{u}}{\partial t} + (\mathbf{u}.\nabla)\mathbf{u}] = \mathbf{f} + \nabla.\overline{\overline{\boldsymbol{\sigma}}}^a = \mathbf{f} - \nabla p^a + \eta_f \nabla^2 \mathbf{u} \qquad (2.14)$$

with ρ, the density of the fluid, $\mathbf{f}$ the external body force and η_f the dynamic viscosity of the fluid. $\mathbf{u}$ is the velocity vector of the fluid and $\overline{\overline{\boldsymbol{\sigma}}}$ is the stress tensor (this stress tensor belongs to the fluid and is different from the one in Eq. ?? which belongs to dry granular flows). Superscript a stands for "absolute", meaning absolute pressure and absolute stress tensor. Considering Newtonian constitutive law, which implies symmetry of the stress tensor, we have:

$$\overline{\overline{\boldsymbol{\sigma}}}^a = -p^a\overline{\overline{\mathbf{I}}} + 2\eta_f\overline{\overline{\mathbf{E}}} \qquad (2.15)$$

where $\overline{\overline{\mathbf{I}}}$ and $\overline{\overline{\mathbf{E}}}$ are the identity and the strain-rate tensors, respectively. In a three-dimensional flow, where all three components of the velocity vector (u_x, u_y, u_z) are non-zero, $\overline{\overline{\mathbf{E}}}$ is expressed as:

$$\overline{\overline{\mathbf{E}}} = \begin{bmatrix} \frac{\partial u_x}{\partial x} & \frac{1}{2}(\frac{\partial u_x}{\partial y} + \frac{\partial u_y}{\partial x}) & \frac{1}{2}(\frac{\partial u_x}{\partial z} + \frac{\partial u_z}{\partial x}) \\ \frac{1}{2}(\frac{\partial u_y}{\partial x} + \frac{\partial u_x}{\partial y}) & \frac{\partial u_y}{\partial y} & \frac{1}{2}(\frac{\partial u_y}{\partial z} + \frac{\partial u_z}{\partial y}) \\ \frac{1}{2}(\frac{\partial u_z}{\partial x} + \frac{\partial u_x}{\partial z}) & \frac{1}{2}(\frac{\partial u_z}{\partial y} + \frac{\partial u_y}{\partial z}) & \frac{\partial u_z}{\partial z} \end{bmatrix} \qquad (2.16)$$

In Eq. 2.14, the term $\frac{\partial \mathbf{u}}{\partial t} + (\mathbf{u}.\nabla)\mathbf{u}$ represents inertial effects while $\eta_f \nabla^2 \mathbf{u}$ represents viscous effects. The dimensionless number showing the comparison between these two effects is called the *Reynolds* number [28, 29],

$$Re = \frac{\rho u L}{\eta_f} \qquad (2.17)$$

where L is a characteristic length scale and $u = |\mathbf{u}|$. The magnitude of the Re number explains which of the effects are more dominating. If $Re \ll 1$, the viscous terms will

be dominating and the inertial terms on the left side of Eq. 2.14 can be neglected. So, Eq. 2.14 can be simplified to:

$$-\mathbf{f} = \nabla.\overline{\overline{\boldsymbol{\sigma}}}^a = -\nabla p^a + \eta_f \nabla^2 \mathbf{u} \tag{2.18}$$

This regime of the fluid flow is called *Stokes* flow (also named *Creeping* flow). There are some special features about Stokes flow among which we can mention: linearity (*i.e.* fluid velocity is linearly dependent on the magnitude of the forcing, due to eliminating non-linear inertial terms), reversibility (*i.e.* motions are reversible in the driving force) and instantaneity (*i.e.* there is no time and history in stokes flow)[28, 30].

2.4.1 Single isotropic/anisotropic particle in a fluid

In order to approach the case of suspensions with many particles suspended in a fluid, we start from a simple case of one particle in a viscous fluid. We assume the particle has the same density as the fluid, so we don't have any creaming or sedimentation effect. A fluid motion near a point $\overline{\overline{\mathbf{x}}}_0$ can be approximated by a truncated Taylor expansion $\mathbf{u}^\infty(\overline{\mathbf{x}}) = \mathbf{u}^\infty(\overline{\mathbf{x}}_0) + \nabla\mathbf{u}^\infty(\overline{\mathbf{x}}_0)(\overline{\mathbf{x}} - \overline{\mathbf{x}}_0)$, assuming that $(\overline{\mathbf{x}} - \overline{\mathbf{x}}_0)$ is small enough that we can neglect the higher order terms in the expansion. The notation $\mathbf{u}^\infty(\overline{\mathbf{x}})$ is used to show the velocity field when there is no disturbance from the particle. In this sense, the flow will be the superposition of a uniform flow and a linearly varying velocity field. If we assume $\overline{\overline{\mathbf{x}}}_0$ to be at the origin and call $\mathbf{u}^\infty(\overline{\mathbf{x}}_0) = \mathbf{U}^\infty$, we get $\mathbf{u}^\infty(\overline{\mathbf{x}}) = \mathbf{U}^\infty + \nabla\mathbf{u}^\infty(0)(\overline{\mathbf{x}})$. The velocity gradient $\nabla\mathbf{u}^\infty$ can be re-written in form of a strain-rate tensor plus a rotation-rate tensor, *i.e.* $\nabla\mathbf{u}^\infty = \overline{\overline{\mathbf{E}}}^\infty + \overline{\overline{\boldsymbol{\Omega}}}^\infty$. The strain-rate tensor was defined earlier in Eq. 2.19 and for $\overline{\overline{\boldsymbol{\Omega}}}^\infty$ we have:

$$\overline{\overline{\boldsymbol{\Omega}}} = \begin{bmatrix} 0 & \frac{1}{2}\left(\frac{\partial u_x}{\partial y} - \frac{\partial u_y}{\partial x}\right) & \frac{1}{2}\left(\frac{\partial u_x}{\partial z} - \frac{\partial u_z}{\partial x}\right) \\ \frac{1}{2}\left(\frac{\partial u_y}{\partial x} - \frac{\partial u_x}{\partial y}\right) & 0 & \frac{1}{2}\left(\frac{\partial u_y}{\partial z} - \frac{\partial u_z}{\partial y}\right) \\ \frac{1}{2}\left(\frac{\partial u_z}{\partial x} - \frac{\partial u_x}{\partial z}\right) & \frac{1}{2}\left(\frac{\partial u_z}{\partial y} - \frac{\partial u_y}{\partial z}\right) & 0 \end{bmatrix} \tag{2.19}$$

So, we can see the problem as the superposition of three simpler cases, *i.e.* a particle in a uniform flow, a particle in solid rotation, and a particle in pure straining. For each problem, we have the linearized momentum equation 2.18 and the corresponding boundary conditions (at the surface of the particles and far from it) to find the solution for the pressure and the velocity fields. For the case of a spherical particle, solid rotation of the fluid around the particle in Stokes regime, induces no pressure

field and leads to a velocity field that decays as r^{-2} (see [30] for more details). If the uniform flow of a fluid past a particle is considered, the boundary conditions at the surface of the particle change, and the pressure then decays as r^{-2} and the dominant portion of the velocity decays as r^{-1}. The third case of straining will lead to a pressure field decaying as r^{-3} and a velocity field decaying as r^{-2} in its dominant term. Having the velocity and the pressure fields, one can get the stress field from Eq. 2.15 and the hydrodynamic force on the particle [30, 31]:

$$\mathbf{F}^{\mathfrak{h}} = \int_{S_p} \overline{\overline{\boldsymbol{\sigma}}}^a . \mathbf{n} \, dS \qquad (2.20)$$

We next consider the torque calculated as:

$$\mathbf{T}^{\mathfrak{h}} = \int_{S_p} \overline{\overline{\mathbf{x}}} \times \overline{\overline{\boldsymbol{\sigma}}}^a . \mathbf{n} \, dS \qquad (2.21)$$

In the case of a spherical particle, it can be shown that the hydrodynamic force in the stokes flow is:

$$\mathbf{F}^{\mathfrak{h}}_{\mathbf{s}} = 3\pi\eta_f d(\mathbf{u}^{\infty} - \mathbf{u}^p) \qquad (2.22)$$

with d being the particle diameter, $\mathbf{u}^{\infty}$ and $\mathbf{u}^p$ are the fluid and the particle velocity, respectively. The subscript $\mathbf{s}$ shows that, this is the hydrodynamic force on a spherical particle. Similarly, there will be a hydrodynamic torque on the spheres:

$$\mathbf{T}^{\mathfrak{h}}_{\mathbf{s}} = \pi\eta_f d^3(\boldsymbol{\omega}^{\infty} - \boldsymbol{\omega}^p) \qquad (2.23)$$

where $\boldsymbol{\omega}^{\infty}$ is the vorticity of the fluid and $\boldsymbol{\omega}^p$ is the angular velocity of the particles.

If instead of a sphere, the particle is a prolate spheroid (ellipsoid) (see Fig. 2.4 for a 2D illustration), with a and b as the major and the minor axes, respectively, the equations become more complicated due to the anisotropy of the particle. However, the superposition principle in the linear stokes flow is still valid [31]. So, we can decompose the flow around the ellipsoid into a uniform flow plus a shear flow. Since we are dealing with an anisotropic particle here, we also need to consider separately
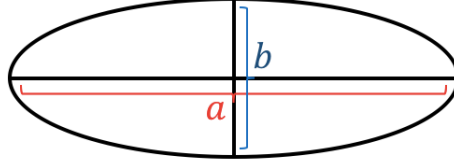
Figure 2.4: Schematic view of an elliptical particle with its major and minor axes.

the rotation of the ellipsoid in the calculation of the hydrodynamic torque, since the particle rotation also contributes to the hydrodynamic torque. Using Eq. 2.13 and 2.18 and applying the superposition principle, the hydrodynamic force on the ellipsoid in the Stokes flow is calculated as:

$$\mathbf{F}_{\mathbf{e}}^{\mathfrak{h}} = 6\pi\eta_f a[c_{fa}(\mathbf{u}^{\infty,a} - \mathbf{u}^{p,a}) + c_{fb}(\mathbf{u}^{\infty,b} - \mathbf{u}^{p,b})] \tag{2.24}$$

In a similar fashion, the hydrodynamic torque will be [31, 32]:

$$\mathbf{T}_{\mathbf{e}}^{\mathfrak{h}} = 8\pi\eta_f ab^2[(c_{Ma}|e_{p,\hat{\mathbf{x}}}|^2 + c_{Mb}|e_{p,\hat{\mathbf{y}}}|^2)\boldsymbol{\omega}^{\infty} - c_{Mr}\boldsymbol{\omega}^p] \tag{2.25}$$

where $\hat{\mathbf{x}}$ and $\hat{\mathbf{y}}$ are the unit vectors in x and y directions, respectively, $\mathbf{u}^p$ and $\boldsymbol{\omega}^p$ are the translational and angular velocity of the particle, $\mathbf{e}_p = (e_{p,\hat{\mathbf{x}}}, e_{p,\hat{\mathbf{y}}})$ is its unit direction vector along the major axis and $\mathbf{u}^{p,a} = (\mathbf{u}^p.\mathbf{e}_p)\mathbf{e}_p$ and $\mathbf{u}^{p,b} = \mathbf{u}^p - \mathbf{u}^{p,a}$ are the particle's velocity in major and minor axes directions, respectively. $\mathbf{u}^{\infty}$ and $\boldsymbol{\omega}^{\infty}$ is the fluid's linear and angular velocities, respectively. Boundary conditions such as the no slip condition on the surface of the ellipsoid and also the conditions far from the particle, lead to the different c coefficients to be determined as (see Ref. [31]): $c_{fa} = \frac{8}{3}e^3[-2e + (1 + e^2)\log(\frac{1+e}{1-e})]^{-1}$, $c_{fb} = \frac{16}{3}e^3[2e + (3e^2 - 1)\log(\frac{1+e}{1-e})]^{-1}$, $c_{Ma} = c_{fa}$, $c_{Mb} = (1 - e^2)^{-1}c_{fa}$, and $c_{Mr} = \frac{4}{3}e^3(\frac{2-e^2}{1-e^2})[-2e + (1 + e^2)\log(\frac{1+e}{1-e})]^{-1}$. $e = \sqrt{(1 - \alpha^{-2})}$ is the eccentricity of the ellipsoid with $\alpha = a/b$ being the aspect ratio of the particle. In paper I we did 2D simulations of suspensions containing elliptical particles and equations 2.24 and 2.25 need to be adjusted for 2D simulations accordingly which will be discussed in more in the next chapter.

2.4.2 Towards dilute suspensions

Now we go beyond the problem of a single particle in a fluid, where we consider dilute suspensions. In a shear flow, the particle can freely rotate which creates no

disturbance in the flow. However, the particle's resistance to the staining component of the shearing flow, results in a disturbance flow, which increases the dissipation of energy in the suspension, *i.e.* the effective viscosity of the of the suspension η increases with increasing number of solid particles in the suspension ϕ. So, the suspension viscosity can be written as:

$$\eta = \eta_f g(\phi) \tag{2.26}$$

where η_f is the fluid viscosity (typical values for the viscosity of water is 10^{-3} Pa.s and for honey is between 1.76 and 252.6 Pa.s) and $g(\phi)$ is an increasing function of the packing fraction. In order to know $g(\phi)$ for dilute suspensions, we start from Eq. 2.15 with an extra term for the contribution of the particles to the stress:

$$\overline{\overline{\sigma}}^a = -p^a \overline{\overline{\mathbf{I}}} + 2\eta_f \overline{\overline{\mathbf{E}}} + \overline{\overline{\sigma}}^p \tag{2.27}$$

where $\overline{\overline{\sigma}}^p$ is the particle contribution to the stress, which is given by fluid-particle stress since particles in the dilute regime have no collisions:

$$\overline{\overline{\sigma}}^p = 5\phi\eta_f \overline{\overline{\mathbf{E}}} \tag{2.28}$$

So, the total stress is given as:

$$\overline{\overline{\sigma}}^a = -p^a \overline{\overline{\mathbf{I}}} + 2\eta_f [1 + \frac{5}{2}\phi]\overline{\overline{\mathbf{E}}} \tag{2.29}$$

Looking at Eq. 2.29 and the shear stress of a suspension we have $g(\phi) = 1 + 5\phi/2$, which the expression give by Einstein[30, 33, 34]. The Einstein viscosity can only predict the viscosity for very dilute suspension up to volume fraction of about 0.05. If the volume fraction increases further, pair interaction between the particles become significant and a second order contribution of ϕ needs to to be taken into account in the viscosity calculation.

2.4.3   Dense suspensions and $\mu(J)$ rheology

In the concentrated suspensions particularly those close to jamming packing fraction, direct particle contacts become dominant in the rheological response[34]. So, it seems
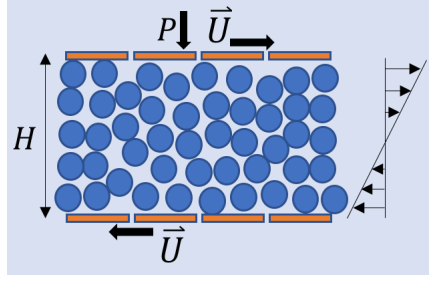
Figure 2.5: Paradigmatic configurations of pressure-imposed shear of a suspension.

there is no direct path to reach dense suspension rheology from it mechanical response in the dilute regime. The shear stress in the dense regime can still be written with a linear dependence on the shear rate [34],

$$\tau = \eta_f g_1(\phi)\dot{\gamma} \qquad (2.30)$$

In general, it's difficult to find an analytical expression for $g_1(\phi)$ for dense suspensions near jamming. However, there are empirical functions to describe the relation between the viscosity and the packing fraction [34]. One of such functions is:

$$\eta/\eta_f = g_1(\phi) \sim (\phi_c - \phi)^{-n} \qquad (2.31)$$

with ϕ_c being the jamming packing fraction and n a positive empirical constant. A similar relation to Eq. 2.30 can be constructed for pressure as:

$$P = \eta_f g_2(\phi)\dot{\gamma} \qquad (2.32)$$

So pressure also scales linearly with the shear rate.

If the dense suspension is sheared at constant particle pressure P as in Fig. 2.5, one can construct a dimensionless number called *viscous number* [25]:

$$J = \frac{\eta_f \dot{\gamma}}{P} \qquad (2.33)$$

.

Assuming the *Stokes number* $St = I^2/J = \rho d^2\dot{\gamma}/\eta_f$ is small (since the particles are neutrally buoyant *Stokes number* is the same as *Reynolds number* if we use the average particle diameter as the characteristic length), viscous forces are governing at the particle level and the internal time is now described by a viscous scaling $t_{micro} = \eta_f/P$. The system is no longer controlled by the inertial number, but rather viscous number. In a similar manner as in the dry-granular case, constitutive laws as two functions of J are given as:

$$\tau = \mu(J)P \tag{2.34}$$

$$\phi = \phi(J) \tag{2.35}$$

2.5 Oscillatory shear

As mentioned earlier, granular materials belong to the family of amorphous materials. Such systems display characteristic viscoelastic properties. While they can behave elastically as solids (with stress being directly in phase with strain) if they are packed highly dense, they can also respond viscous as liquids (with stress being completely in phase with shear rate) if the grains are not sufficiently dense [35]. Oscillatory shear flows have been widely used as a powerful tool to investigate such viscoelastic features. Oscillatory shear can be applied to the system via a periodic strain or shear, etc. As an example, in a planar shear set-up, a sinusoidal strain, $\gamma(t) = \gamma_0 \sin(\omega t)$, is applied to the sample, where γ_0 is the amplitude of the strain and ω is the oscillation frequency. The shear rate will then be, 90 degrees shifted in phase (compared to the strain), a cosine function, $\dot{\gamma}(t) = \dot{\gamma}_0 \cos(\omega t)$, where $\dot{\gamma}_0 = \omega\gamma_0$ is the corresponding shear rate magnitude. The stress response of the sample $\sigma(t)$ is then measured. In the linear response regime, the expected response of a pure elastic material is:

$$\sigma(t) = \omega\eta''\gamma(t) = \eta''\dot{\gamma}_0 \sin(\omega t) \tag{2.36}$$

and for a purely viscous material, we have:

$$\sigma(t) = \eta'\dot{\gamma}(t) = \eta'\dot{\gamma}_0 \cos(\omega t) \tag{2.37}$$

where η'' and η' are the corresponding elastic and viscous viscosities, respectively. The response for a viscoelastic material is then a linear combination of the viscous and the

elastic response, $\sigma(t) = \eta'' \dot{\gamma}_0 \sin(\omega t) + \eta' \dot{\gamma}_0 \cos(\omega t)$ with $\eta' = \frac{\int_0^{2\pi/\omega} \sigma(t) \cos(\omega t)\, dt}{\dot{\gamma}_0 \int_0^{2\pi/\omega} \cos^2(\omega t)\, dt}$, $\eta'' = \frac{\int_0^{2\pi/\omega} \sigma(t) \sin(\omega t)\, dt}{\dot{\gamma}_0 \int_0^{2\pi/\omega} \sin^2(\omega t)\, dt}$, respectively. In this case we will have a complex viscosity defined as $\eta^* = \eta' - i\eta''$ [36, 37, 38]. In a manner similar to the dimensionless viscous number for suspensions in the steady viscous regime, we can define a shear-rate-weighted average viscous number J' as $J' = \frac{\eta_f \int_0^{2\pi/\omega} \left(\frac{\dot{\gamma}}{P}\right) \dot{\gamma}(t)\, dt}{\int_0^{2\pi/\omega} |\dot{\gamma}(t)|\, dt}$ [38]. J' serves as a measure of the average shear rate (formally shear-rate-weighted) of the suspension and is directly related to how far one is from a suspension's jamming point (*i.e.*, $\phi_c - \phi$).

The rheology of granular materials can be quite complicated at unsteady shear conditions, showing non-trivial transient behaviors [39, 40, 41]. For instance, it has been shown that oscillatory shear perpendicular [42, 43, 44] or parallel to the primary constant shear [38] can increase the flowability of particle flows by reducing the viscosity [38, 44]. The phenomenon is not yet completely understood. However, it is generally attributed to a restructuring of the microstructure [38] which, for instance, at orthogonal shear flows, can happen through a tilting and ultimate breakage of the force chains [42]. It has also been found that at small oscillatory magnitudes, particles can create reversible trajectories, meaning that they come into an absorbing state in which they manage to avoid contact with other particles. So, the decrease in the number of particle contacts leads to a decrease in the contact stress [44, 45, 46, 47]. Under oscillation, it has also been observed that the jamming packing fraction is shifted to a higher value, denoting that shear jammed configurations can start to flow [44]. Considering granular materials with anisotropic particles can open new windows towards more interesting and complicated phenomena in oscillatory rheology, specifically related to the particle shapes [48, 49].

2.6   Segregation effects

Granular materials segregate in separate regions when sheared, stirred, shaken, tumbled, etc. Small differences in particle properties and dynamics of the flow can lead to segregation, a complex and common phenomenon without parallel in fluids [50, 51, 52, 53, 54].

Despite decades of research on granular flow-driven segregation, there are still many open questions in this area such as the existence of global segregation mechanisms and the possibility of developing a consolidated model to describe the phenomenon [55].
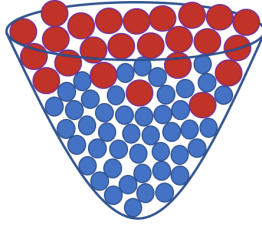
Figure 2.6: Schematic view illustrating Brazil-nut effect with large granules accumulating on top of small grains.

Among various mechanisms that prevent a homogeneous mixture of grains, size segregation turns out to be very important. Different physical mechanisms have been suggested for size segregation, some of which are percolation, sifting, squeeze expulsion, convective motion of the grains and surface flow effects [50, 52, 53, 56, 57, 58, 59, 60]. Many studies have been focused on vertically shaken granular mixtures, where the larger grains will end up on top of the smaller ones, the phenomenon referred to as "Brazil-nut effect" [61, 62, 63], see Fig. 2.6.

Although in many industrial and rheological applications, granular particles have irregularities in their shapes, segregation due to shape variation of the grains has not been very frequently investigated. Most studies focused on modeling spherical (circular) particles. Anisotropy of the particles can, however, drive significant macroscopic differences with mixtures of purely spherical (circular) grains. Therefore, studying the effect of shape anisotropy on the segregation of granular materials can help us have a deeper understanding of the phenomenon.

Some studies use continuum segregation models which are configuration-dependent since altering the boundary conditions will change the closure schemes of the equations [64, 65, 66]. However, to inspect the phenomenon at the particle scale, the latest studies have attempted characterizing forces separately on various particle species of the flow [67, 68] which then have led to developing segregation force models applicable to numerous configurations[68, 69]. What we do in our study is based on the second approach using a "restoring force" in a bi-disperse mixture of big and small discs to help the segregated configuration return to its homogenized state. We explain more about the details of the technique we used, in the Results chapter.

Chapter 3

Numerical modeling and simulation technique

Analytical solutions to the mechanical behavior of the granular materials are obtained by solving the governing equations describing the dynamics of the system. So, a full set of equations including Newton's second law of motion for the particles and the Navier-Stokes equations for the interstitial fluid need to be solved simultaneously. Then the equations are interconnected through the boundary conditions, such as the no-slip condition on the surface of the particles and on the rough confining walls. However, analytical solutions are greatly costly computationally when it comes to studying granular and dense suspension flows with a large number of particles. Therefore, the necessity to use numerical approximations to lower the computational cost is understandable.

3.1   Discrete element method

The discrete element method (DEM) is the most attractive numerical method used by researchers and engineers to successfully design, analyze and optimize granular materials and dense suspensions, comprising of a continuum fluid phase and discrete particles [70, 71, 72, 73, 74]. The DEM simulation involves the assignment of co-ordinates and velocities to each particle, following which the forces acting on each particle are determined using corresponding models. The details regarding the forces and dynamics involved in the simulation are discussed in the subsequent section. The calculation of forces and propagation of the system is repeatedly carried out until the simulation ends. To ensure that unphysical configurations resulting from large time
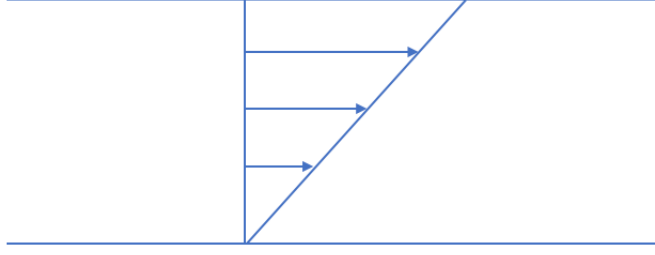
Figure 3.1: Sketch showing velocity profile of the fluid in simple shear simulations

steps are avoided, the time step dt is always smaller than the time taken for one collision. This allows for a clearer microscopic picture of each particle. In the works presented here, two-dimensional DEM simulations are run, where particles are disks or ellipses. Fluids are simulated implicitly, represented by a simple shear velocity profile, as illustrated in Fig. 3.1. So, instead of solving for the fluid velocity at each point, the fluid is represented by a locally averaged velocity. However, particles are handled individually and their equations of motion are solved separately. Although continuum-based methods such as the finite element method (FEM) [75] and meshless methods [76] can also be used to describe granular materials, they are usually difficult to model large deformations and displacements as well as segregation and mixing of granular flows with.

3.2 Forces

3.2.1 Contact forces

Due to the high packing fractions present in dense suspensions, contact forces between colliding particles play a dominant role. To model this contact force, a damped harmonic spring is utilized. When considering the collision of two grains, i, and j, the contact force between them is given by the following equation [77]:

$$\mathbf{f}^{ij} = \mathbf{f}_n^{ij} + \mathbf{f}_t^{ij} = (k_n\delta_n^{ij} + \zeta_n\dot{\delta}_n^{ij})\mathbf{n}^{ij} + (k_t\delta_t^{ij} + \zeta_t\dot{\delta}_t^{ij})\mathbf{t}^{ij}, \qquad (3.1)$$

Here, k_n represents the normal spring constant, ζ_n represents the normal dissipation constant, δ_n^{ij} is the normal overlap between the two particles, $k_t = k_n/2$ represents the tangential spring constant, δ_n^{ij} represents the relative tangential displacement between the grains i and j, ζ_t represents the tangential dissipation constant, n^{ij} denotes

the normal unit vector, t^{ij} denotes the tangential unit vector, $\dot{\delta}_n^{ij}$ and $\dot{\delta}_t^{ij}$ indicate the time derivatives. It is important to note that in our simulations, the particles are considered to be non-deformable and rigid with a spring constant of $k_n/P > 10^3$, where P is the pressure in the system. Additionally, overlaps between multiple particles are ignored due to the high rigidity of the particles and their low likelihood of occurring.

Relative tangential displacement δ_t^{ij} can be defined as

$$\delta_t^{ij} = \int_0^t u_t^{ij} \, dt \,, \tag{3.2}$$

where u_t^{ij} is the tangential projection of the relative velocity u^{ij} between two particles i and j.

$$u_t^{ij} = \mathbf{t}^{ij} . \mathbf{u}^{ij}, \tag{3.3}$$

The Coulomb friction restricts the maximum value of the tangential force f_t^{ij},

$$|\mathbf{f}_t^{ij}| \leq \mu_p |\mathbf{f}_n^{ij}|, \tag{3.4}$$

where f_t^{ij} is the normal force and μ_p is the corresponding value of the friction coefficient that reflects the surface properties of the particles. A standard value for μ_p is 0.4, which is applicable to surfaces such as steel, glass, chromium, and nylon-66, as reported in reference [78].

The normal dissipation constant ζ_n can be defined as follows:

$$\zeta_n = -\frac{2\sqrt{m_{ij}k_n}\ln e}{\sqrt{\pi^2 + (\ln e)^2}}, \tag{3.5}$$

where m_{ij} the reduced mass, denoted by $m_{ij} = m_i m_j/(m_i + m_j)$, and the restitution coefficient, e, which characterizes the velocity difference before and after a collision, play key roles in describing dissipative collisions. The tangential dissipation constant is defined analogously by replacing k_n in Eq. 3.5 with k_t. The dissipative nature of collisions can be intuitively understood by considering the trajectory of a bouncing ball, as illustrated in Fig. 3.2. For $e < 1$ energy is lost during each collision. In our simulation of dense suspensions in the viscous regime, the contact force is balanced by the viscous force, and we have set $e = 1$ for numerical reasons.
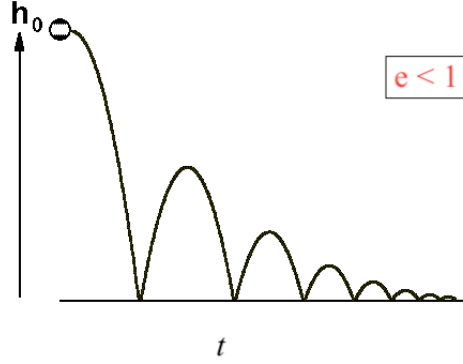
Figure 3.2: Schematic view of a bouncing ball trajectory on a hard surface with a restitution coefficient $e < 1$.

3.2.2 Fluid force

In addition to contact forces, particles are subjected to hydrodynamic forces from fluid fields, as discussed in chapter 2. In the simulations, the fluid is modeled as a continuum, and it is assumed that the particles do not perturb the laminar flow of the fluid. As a result, the fluid force and torque on discs are calculated using adjusted Eq. 2.22 and 2.23, respectively for 2D simulations, yielding the following expressions.

$$\mathbf{F}_{\mathbf{s}}^{\natural} = 3\pi\eta_f(\mathbf{u}^{\infty} - \mathbf{u}^p),\tag{3.6}$$

$$\mathbf{T}_{\mathbf{s}}^{\natural} = \pi\eta_f d^2(\boldsymbol{\omega}^{\infty} - \boldsymbol{\omega}^p),\tag{3.7}$$

and in the case of elliptical particles, Eq. 2.24 and 2.25 are adjusted for 2D simulations to calculate the hydrodynamic force and torque as follows:

$$\mathbf{F}_{\mathbf{e}}^{\natural} = 6\pi\eta_f[c_{fa}(\mathbf{u}^{\infty,a} - \mathbf{u}^{p,a}) + c_{fb}(\mathbf{u}^{\infty,b} - \mathbf{u}^{p,b})],\tag{3.8}$$

$$\mathbf{T}_{\mathbf{e}}^{\natural} = 8\pi\eta_f ab[(c_{Ma}|e_{p,\hat{\mathbf{x}}}|^2 + c_{Mb}|e_{p,\hat{\mathbf{y}}}|^2)\boldsymbol{\omega}^{\infty} - c_{Mr}\boldsymbol{\omega}^p],\tag{3.9}$$

For the description of the parameters in the above four equations, see Eq. 2.22, 2.23, 2.24 and 2.25 in chapter 2. As observed from Eq. 3.6 to 3.9 the hydrodynamic forces and torques in 2 dimensions slightly differ compared to those in 3 dimensions.

3.2.3 Lubrication forces

Lubrication force refers to the force generated by the hydrodynamic pressure of the interstitial fluid that is expelled from the region between two solid surfaces [79]. In the suspension simulations, the particles are also subjected to pair lubrication forces. A regularised lubrication model is employed to calculate the force. The equations utilized for determining the lubrication forces between particle i and j are as follows [80, 81]:

$$\mathbf{f}(h_{ij})^{ij}_{\mathbf{lub,n}} = \left[-\frac{3}{8}\pi\eta_f d_{ij} \frac{(\mathbf{u}^p_i - \mathbf{u}^p_j) \cdot \mathbf{n}_{ij}}{h_{ij} + \delta} \right] \mathbf{n}_{ij}, \qquad (3.10)$$

$$\mathbf{f}(h_{ij})^{ij}_{\mathbf{lub,t}} = \left[-\frac{1}{2}\pi\eta_f \ln\left(\frac{d_{ij}}{2(h_{ij}+\delta)}\right) (\mathbf{u}^p_i - \mathbf{u}^p_j) \cdot \mathbf{t}_{ij} \right] \mathbf{t}_{ij}, \qquad (3.11)$$

Eq. 3.10 and 3.11 indicate that the calculation of lubrication forces between particles i and j involves the determination of gap distance, h_{ij}, as well as the effective grain diameter, $d_{ij} = \frac{2d_i d_j}{d_i + d_j}$, and the normal and tangential unit vectors, $\mathbf{n}_{ij}$ and $\mathbf{t}_{ij}$, respectively. Additionally, a regularization length, denoted by δ, is incorporated into the model, with a value equal to 5% of the particle diameter. In real suspensions, this parameter can be linked to the slip length, grain roughness, or the range over which elastic deformation of grains occurs [81, 82]. In paper I, the results will not change with/without the lubrication forces. So, to reduce our computational cost we run the simulations without considering the lubrication forces.

3.3 Dynamics

3.3.1 Equations of motion

Newton's second law of motion can be used to depict the dynamics of particles immersed in a fluid

$$m_i \frac{d\mathbf{u}_i}{dt} = \mathbf{f}^{\mathfrak{h}}_i + \mathbf{f}^{ext}_i + \sum_j \mathbf{f}^c_{ij}, \qquad (3.12)$$

The formula involves three distinct forces, namely $\mathbf{f}_i^{\natural}$, which represents the viscous force dependent on both the position and velocity of the particle, $\mathbf{f}_i^{ext}$, which is the external force acting on the particle, and $\mathbf{f}_{ij}^c$, which denotes the contact force that also depends on the particle's position. m_i is the mass of particle i and $\frac{d\mathbf{u}_i}{dt}$ is the linear acceleration of particle i (sometimes shown as a_i as well). If the particles are not immersed in a fluid, as they are in the dry granular flows, the term $\mathbf{f}_i^{\natural}$ will not exist in Eq. 3.12 and the force and the torque equations will be

$$m_i \frac{d\mathbf{u}_i}{dt} = \mathbf{f}_i^{ext} + \sum_j \mathbf{f}_{ij}^c, \qquad (3.13)$$

$$I_i \alpha_i = \tau_i^{ext} + \sum_j \tau_{ij}^c, \qquad (3.14)$$

where τ_i^{ext}, and τ_{ij}^c are the external and the contact torques. I_i is the mass moment of inertia of a particle about the normal axis to $x - y$ plane through its center of mass and α_i is the granule's angular acceleration.

The position and velocity of the particle can be computed by integrating Eq. 3.12 using the Verlet algorithm, as outlined in reference [83],

$$\mathbf{r}_i(t + \Delta t) = 2\mathbf{r}_i(t) - \mathbf{r}_i(t - \Delta t) + \frac{1}{m_i}\left(\mathbf{f}_i^{\natural} + \mathbf{f}_i^{ext} + \sum_j \mathbf{f}_{ij}^c\right)\Delta t^2, \qquad (3.15)$$

$$\mathbf{u}_i(t + \Delta t) = \frac{\mathbf{r}_i(t + \Delta t) - \mathbf{r}_i(t - \Delta t)}{2\Delta t} + \frac{1}{m_i}\left(\mathbf{f}_i^{\natural} + \mathbf{f}_i^{ext} + \sum_j \mathbf{f}_{ij}^c\right)\Delta t, \qquad (3.16)$$

where $\mathbf{r}_i(t + \Delta t)$ and $\mathbf{u}_i(t + \Delta t)$ are the new velocity and position, $\mathbf{r}_i(t)$ is the current position, and $\mathbf{r}_i(t - \Delta t)$ is the old position. Δt is the time step. For the orientation and angular velocity of the grains, similar equations are used using the moment of inertia of the particles.

3.3.2 Overdamped Langevin dynamics

If the suspension flow is in the viscous regime, the dynamics of the particles are over-damped which leads to force and torque balance [84]

$$\mathbf{f}_i^{\mathfrak{h}} + \mathbf{f}_i^{ext} + \sum_j \mathbf{f}_{ij}^c = 0, \tag{3.17}$$

$$\tau_i^{\mathfrak{h}} + \tau_i^{ext} + \sum_j \tau_{ij}^c = 0, \tag{3.18}$$

where $\mathbf{f}_i^{\mathfrak{h}}$, $\mathbf{f}_i^{ext}$, and $\mathbf{f}_{ij}^c$ were described in Eq. 3.12 while $\tau_i^{\mathfrak{h}}$, τ_i^{ext}, and τ_{ij}^c are the torques resulting from hydrodynamic, external and contact forces, respectively.

3.4   Technical details

In the simulations, we might have discs or ellipses. Fig. 3.3, taken from size segregation simulations, depicts a simulation box containing $\sim$ 1800 size bi-disperse discs. The average diameter of the particles is represented as d and all length scales involved in the simulations are expressed in units of d. The walls of the simulation consist of the same type of particles as the flowing ones but are glued together and marked in red in Fig. 3.3. If not bi-disperse disc mixtures (as in paper ii where we study size segregation), for elliptical particles the particle sizes are described by a flat distribution with 50% polydispersity in the major axis (as in paper i). During the pressure control simulations, the bottom wall remains fixed along the y-axis while the top wall is adjustable with an imposed pressure P on the y-axis that balances the normal stress along the y-direction at steady-state. At a constant shear rate, the top wall moves at a constant velocity along the x-axis, resulting in a strain in the system. At oscillatory shear simulations, an oscillatory velocity is applied to the top wall resulting in an oscillatory shear rate. The numerical unit for stress is P and the time unit is $1/\dot{\gamma}$. The fluid within the simulation is modeled as a continuum with a velocity profile. The fluid has a no-slip boundary at the wall. Additionally, periodic boundary conditions are applied along the x-axis, and interactions between the particles are calculated using the nearest image convention, as shown in Fig. 3.4. In the segregation simulations, we also have a gravity field $g(y)$ present whether in y direction, which follows the numerical unit description explained above.
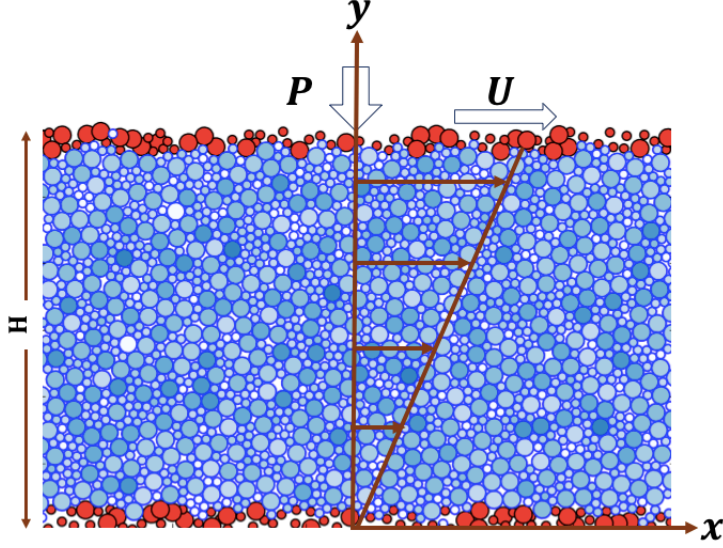
Figure 3.3: A snapshot from size segregation simulations, with x and y-axis illustrated. **P** is the imposed pressure and **U** is the applied velocity on the wall. The crimson arrows illustrate the fluid velocity profile.

In a particle system, the shear stress σ_{xy} and the pressure $P = \frac{1}{2}(\sigma_{xx} + \sigma_{yy})$ are calculated from the particle stress tensor

$$\overline{\overline{\sigma}} = \frac{1}{A} \sum_{i \in A} \mathbf{f}_i \cdot \mathbf{r}_i = \begin{bmatrix} \sigma_{xx} & \sigma_{xy} \\ \sigma_{yx} & \sigma_{yy} \end{bmatrix}, \tag{3.19}$$

in which A is the area where the stresses are sampled, $\mathbf{f}_i$ is the total force acting on particle i and $\mathbf{r}_i$ is its position. $\sigma_{xy} = \sigma_{yx}$ are the shear stresses while σ_{xx} and σ_{yy} are the normal stress along their corresponding axes.

For particle flows, we can measure a granular temperature, which is related to the fluctuations in particle velocities in a granular system and is used to describe the average kinetic energy associated with the random motion of particles. The granular temperature is calculated as $T_{yy}(y) = 1/A \sum_{i \in A} m_i \delta v_{i,yy}^2$, where $\delta v_{i,yy}$ is the velocity fluctuations of particle i in y direction, m_i is the particle mass and A is the area where the temperatures are sampled. The dimensionless temperature is then defined as $\Theta_{yy}(y) = T_{yy}(y)/P(y)$.

For anisotropic particles like ellipses, there are some direction parameters. The nematic order parameter S_2, which is a measure of how aligned the particles are, is taken as the largest eigenvalue of the director tensor $Q^{kl} = 1/N \sum_i (2\mathbf{e}_i^k \mathbf{e}_i^l - \delta_{kl})$, where
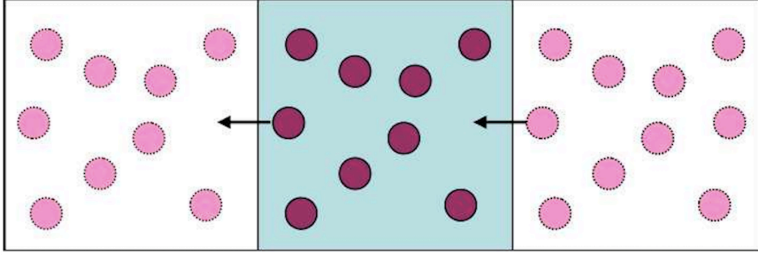
Figure 3.4: Periodic boundary condition in the x-direction between the particles in the simulation box and the particles in the neighboring boxes.

N is the number of particles over which the measure is taken and δ_{kl} the Kronecker delta. The value of S_2 can vary between 0 and 1 for a fully amorphous configuration and a perfect crystalline structure, respectively. $\mathbf{e}_i = (e_{i,\hat{\mathbf{x}}}, e_{i,\hat{\mathbf{y}}})$ is each ellipse's unit direction vector along its major axis as also referred to in section 2.4.1.

Another direction parameter for elliptical particles is $\theta_{\mathbf{e}\cdot\hat{y}}$, which is measured as the average particle angle with respect to y direction, normal to the lower surface (see SI of paper 1).

The values reported for each parameter are ensemble averages that are obtained by sampling over the simulations. To make sure that we are not taking into account the transient effects when we study oscillatory shear, we run at least 10 complete periods or a minimum shear strain of 10 should be reached to do sampling. Similarly, when we have gravity in the system, to ensure that steady-state properties are sampled, the minimum shear strain corresponding to the minimum shear rate in the system is kept larger than 3 before we sample the properties.

Chapter 4

Results

4.1 Paper 1: Orientational arrest in dense suspensions of elliptical particles under oscillatory shear flows

Our focus in paper 1 is on investigating the effect of particle shape anisotropy on the rheology of dense non-Brownian suspensions under oscillatory shear.

We used a discrete element method to study the rheology of two-dimensional suspensions consisting of approximately 1000 size-poly-disperse ellipses with an aspect ratio of $\alpha = a/b = 3$. The simulations are pressure-controlled. A macroscopic oscillatory shear rate $\dot{\gamma}(t) = \dot{\gamma}_0 \cos(\omega t)$ is applied to the system, with $\dot{\gamma}_0$ and ω being the amplitude and the frequency of the oscillatory shear, respectively.

The suspension is in the viscous regime. Particles interact via harmonic forces as explained in Eq. 3.1 with restitution parameter $e = 1$. The friction coefficient between the particles is either $\mu_p = 0$ (frictionless) or $\mu_p = 0.4$ (frictional). The interstitial fluid is Newtonian. The viscous force and torque by the background shear flow on the particles are according to Eq. 3.8 and 3.9, respectively. The dynamics of the particles are overdamped which leads to force and torque balance, as described in Eq. 3.17 and 3.18.

We select two preparation protocols for our suspensions. The first one is the presheared preparation protocol. This protocol results in a well-defined orientation of the ellipses. In the second protocol, we have suspensions with randomly oriented ellipses. After the two initial configurations are settled, the system undergoes an oscillatory shear. Direction parameters like the nematic order S_2 and the average orientation angle $\theta_{\mathbf{e}\cdot\hat{y}}$ of the particles are measured as explained in section 3.4 in the previous
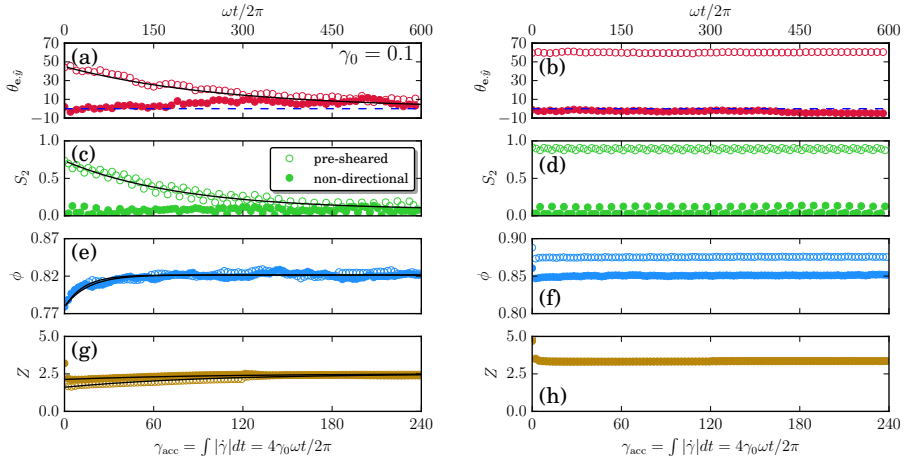
Figure 4.1: The figure shows the evolution of various properties for both frictional and frictionless configu-
rations at a small oscillatory strain ($\gamma_0 = 0.1$) and $J' \simeq 0.1$. The left column corresponds to the
frictional configuration with a coefficient of friction of $\mu_p = 0.4$, while the right column corre-
sponds to the frictionless configuration with $\mu_p = 0$. The properties shown are the direction angle
$\theta_{\mathbf{e}\cdot\hat{y}}$ (in degrees), nematic ordering S_2, packing fraction ϕ, and number of contacts Z. The empty
and full symbols correspond to pre-sheared and non-directional preparations, respectively. The
black lines are the best fits of the relaxations, while the blue dashed lines in the direction angle
plots indicate the zero lines.

chapter.

As discussed in section 2.5, we get a viscoelastic response from the suspension under
oscillatory shear. We also use a shear-rate-weighted average viscous number, J' as a
measure of the average shear rate of the suspension (introduced in section 2.5).

Fig. 4.1 illustrates typical numerical time-evolutions of various parameters, namely
$\theta_{\mathbf{e}\cdot\hat{y}}$, S_2, ϕ, and Z, under oscillatory shear (OS) conditions. These data stem from
two distinct preparation protocols: pre-sheared and random packings, involving both
frictional and frictionless particles, all subjected to a low oscillatory strain ($\gamma_0 = 0.1$).
Initially, the packings are at rest.

In the case of frictional particles, both starting configurations under the same J' con-
verge to a higher packing fraction compared to their steady-shear counterparts. They
also converge to a state of directional disorder characterized by low nematic ordering,
with the average orientation fluctuating around zero. Remarkably, these orientational
values closely match, if not identical, to the initial random configuration, indicating
that the pre-sheared samples relax towards random configurations. The number of
contacts also relaxes quite rapidly and becomes identical for both preparation proto-
cols. Interestingly, this is not the case for frictionless ellipses, where all quantities,
except the number of contacts, remain distinct for the two preparation protocols,
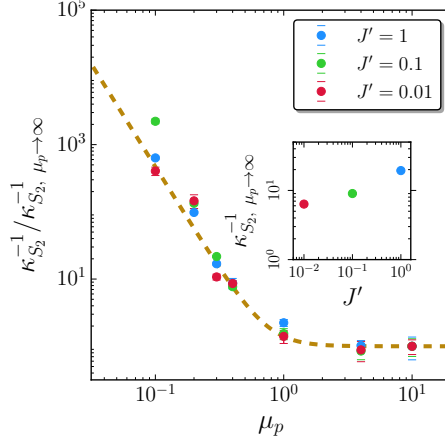showing no detectable relaxation within our numerical time frame.

Figure 4.2: The rescaled relaxation parameter governing the nematic order, denoted as $\kappa_{S_2}^{-1}$, is depicted as a function of μ_p for the pre-sheared configuration, under the condition $\gamma_0 = 0.1$, across various J' values. Each curve corresponding to a specific J' has been normalized by its respective value as $\mu_p \to \infty$. The dashed line signifies the best fit of the data with the relationship $\kappa_{S_2}^{-1} \sim a_{S_2} \mu_p^{-\beta} + c$.

To gain further insight, we estimate the strains over which the various quantities potentially relax. More specifically, to delve further into the role of frictional interaction, we conduct simulations and measure S_2 relaxation strains, starting from pre-sheared configurations, for systems with varying friction coefficients. In Fig.4.2, we observe the relaxation strain in S_2 plotted against the friction coefficient μ_p. The data suggests that the relaxation strains in S_2 might exhibit a divergence following $\kappa_{S_2}^{-1} \sim \mu_p^{-\beta}$. Due to the sharp divergence, it's challenging to determine if this divergence happens at a tiny finite critical friction coefficient $\mu_{p,c}$ or at $\mu_{p,c} = 0$. In our study, the smallest friction coefficient we considered was $\mu_p = 0.1$, associated with the slowest detectable relaxation strains for S_2. So, the friction coefficient threshold to observe orientational arrest must be between 0 and 0.1.

Notably, introducing a finite amount of friction aids the system in relaxing its orientation, akin to a ratcheting process [85]. Beyond $\mu_p = 1$, the relaxation strains stabilize and depend solely on J' and γ_0. Smaller J' values lead to smaller relaxations in terms of strains (as seen in the inset of Fig.4.2), indicating higher packing fractions in these cases, along with a greater number of contacts and collisions per strain.

After establishing that frictionless particles do not conform to a single unique equation of state at low oscillatory strains, we proceed to examine how the complex viscosity changes with packing fraction and γ_0 for our two preparation protocols, in comparison to frictional particles (refer to Fig. 4.3 (a, b)). For both (a) frictional and (b) frictionless ellipses, we observe that the rheological response (i.e., $|\eta^*|$ vs. ϕ) behaves similarly to their corresponding steady shear (SS) cases at high γ_0 values. However,
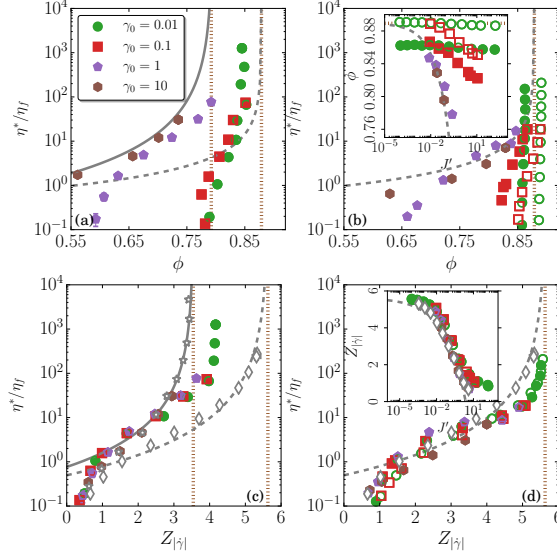
Figure 4.3: (a) and (b) present the normalized complex viscosities $|\eta^*|/\eta_f$ plotted against the packing fraction ϕ for both frictional and frictionless particles, respectively. (c) and (d) show the same viscosities in relation to the number of contacts $Z_{|\dot\gamma|}$. In all figures, open symbols represent pre-sheared preparations, while solid symbols represent non-directional preparations. The solid grey lines and dashed grey lines represent the steady shear viscosity curves for frictional and frictionless particles, respectively. Additionally, the brown dotted vertical lines in (a) and (b) indicate the packing fractions at which steady shear jamming occurs for frictional ($\phi_{c,f}^{SS}$) and frictionless ($\phi_{c,nf}^{SS}$) suspensions. Similarly, in (c) and (d), they mark the steady shear jamming number of contacts for frictional ($Z_{c,f}^{SS}$) and frictionless ($Z_{c,nf}^{SS}$) configurations. The insets in (b) and (d) provide additional details. The inset in (b) shows ϕ as a function of J' for the frictionless ellipses, with the grey dashed line indicating the corresponding steady shear curve. Similarly, the inset in (d) illustrates Z versus J' for the non-frictional particles, where the dashed line denotes the respective steady shear case.

at lower γ_0 values, we observe a lower viscosity compared to the SS case at the same packing fraction, accompanied by an increased shear jamming packing fraction for the frictional particles, denoted as $\phi_{c,f}^{SS} < \phi_{c,f}^{OS}$. These observations align with prior reports for discs [38, 86] and spheres [42, 44].

In contrast to isotropic particles, frictionless ellipses exhibit a rheology that depends on the preparation protocol (compare full and open symbols). Specifically, pre-sheared preparations result in higher shear jamming packing fractions compared to non-directional/random ones. For frictionless ellipses, the non-directional preparation yields a shear jamming point below its corresponding point in SS (i.e., $\phi_{c,nf}^{OS,ran} < \phi_{c,nf}^{SS}$). This indicates the presence of at least two distinct oscillatory shear-jamming points for frictionless elliptical particles. Nevertheless, when the complex viscosity $|\eta^*|/\eta_f$ is plotted against the number of contacts Z in Fig.4.3 (c) and (d), the two protocols for frictionless particles collapse onto each other, despite having different packing fractions and orientational properties.

4.2 Paper II: An iterative method for measuring spatial segregation forces in bi-disperse granular flow mixtures under various gravity fields

In this paper, using DEM, we study two different methods to calculate the restoring forces in size bi-disperse mixtures of big and small discs and compare the range of applicability of the methods in pressure-controlled simulations. The configurations consist of approximately 1750 big and small discs. The relative average packing fractions of big and small discs are $\langle \frac{\phi_b}{\phi_{tot}} = \psi_b \rangle \sim 0.65$ and $\langle \frac{\phi_s}{\phi_{tot}} = \psi_s \rangle \sim 0.35$, respectively. The system is subjected to vertical gravity as well, which can be either a constant or a linearly increasing gravity, always starting at zero at the top. We have periodic boundary conditions in x-direction.

The granular flow is in the inertial regime. Particles interact via harmonic forces as explained in Eq. 3.1 with restitution parameter $e = 0.1$. Coulomb friction constrains the tangential force as described in Eq. 3.4. The particles are either frictionless ($\mu_p = 0$) or frictional ($\mu_p = 0.4$). The dynamics of the discs follow Newton's second law according to Eq. 3.13 and 3.14.

Figure 4.4($\mathbf{a}$) presents a sample snapshot of the investigated mixture, specifically from the Couette flow configuration where the mixture is in a homogeneous state. In Figures 4.4($\mathbf{b}$) and ($\mathbf{c}$), gravity and pressure profiles are depicted over the height of the pile when a constant and a linearly increasing vertical gravity are applied to the system, respectively. The stress tensor and the granular temperature are calculated according to section 3.4 and the inertial number $I(y)$ as explained in section 2.3.1.

In this investigation, we use two distinct methodologies for calculating segregation forces. The approach involves identifying a restoring force profile that counteracts segregation and gives a homogenized mixture, designated as $F_{\mathrm{res},s/b}$. The segregation force will then be the negative of this force, expressed as $F_{\mathrm{seg},s/b} = -F_{\mathrm{res},s/b}$. s/b stands for small or big discs, respectively.

All forces are presented in a rescaled format. Consequently, in the case of a system under constant gravity, we plot $F^*_{res,b/s} = F_{res}/m_{b/s}|g|$, and if the gravity increases linearly, we depict $F^{\dagger}_{res,b/s} = F_{res}/m_{b/s}|g|_{\mathrm{max}}$, where $m_{b/s}$ is the mass of big or small particles, $|g|$ is the magnitude of constant gravity, and $|g|_{\mathrm{max}}$ is the maximum gravity in the case of linearly increasing gravity.
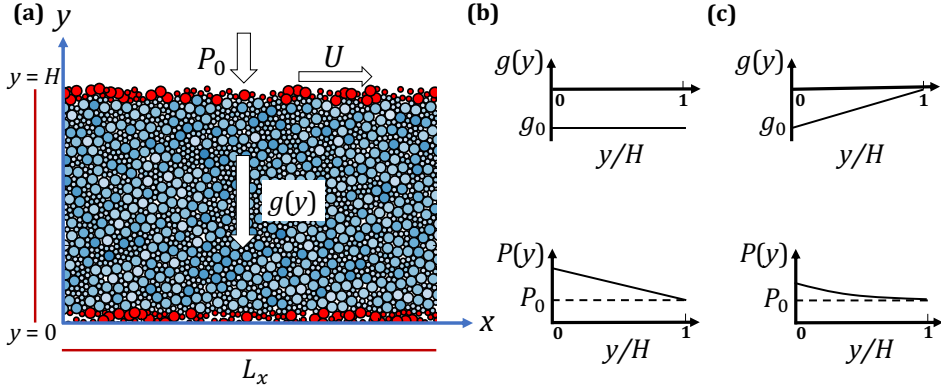
Figure 4.4: a) presents a schematic representation of a granular mixture under investigation. The coordinate axes and boundary conditions are illustrated in the figure, with a gravity field applied to the system. **b)** illustrates a scenario with a constant gravity field, denoted as $g(y) = g_0$, and the corresponding pressure profile. **c)** depicts a scenario with a linearly increasing gravity field, denoted as $g(y) = -(g_0/H)\,y + g_0$, and the corresponding pressure profile.

4.2.1 Harmonic Restoring Forces

The initial technique, referred to as the Harmonic Method (HM), is based on a methodology introduced by a previous study [87] and similarly by [68]. This method employs a spring-like vertical restoring force that is proportional to the difference in the vertical center of mass positions of the two initially mixed species.

The formula for the restoring force on each species, whether big or small (b/s), is given by: $F_{\text{res},b}^{\text{HM}} = -K_r P_0 (\bar{y}_b - \bar{y}_s) \frac{N}{N_b}$ and $F_{\text{res},s}^{\text{HM}} = -F_{\text{res},b}^{\text{HM}} \frac{N_b}{N_s}$ where $\bar{y}_b = 1/N_b \sum_{k \in b}^{N_b} y_k$ represents the center of mass of big discs, and a corresponding expression holds for small particles. Here, and N_b, N_s, and N are the numbers of big particles, small particles, and the total number of particles in the bulk region. K_r is a dimensionless constant set to 0.6. The harmonic restoring forces satisfy force balance, *i.e.*, $F_{\text{res},b}^{\text{HM}} N_b + F_{\text{res},s}^{\text{HM}} N_s = 0$.

4.2.2 Iterative Segregation Method

We introduce an alternative methodology that exhibits broader applicability compared to the initial technique, allowing for the determination of the restoring force distribution over the slab even in the presence of a linearly increasing vertical gravity. In this scenario, we consider a flowing configuration that has already attained a steady-state segregated state under the influence of both gravity and external shear. Our iterative approach aims to estimate the required restoring force for assisting the system in reverting to its mixed state at each update. This is achieved by leveraging the

difference between the slopes of the relative packing fraction profiles of each species in the non-homogeneous configuration and the desired homogeneous mixture, corresponding to pure Couette flow. In this work, we term this approach the Iterative Method (IM).

In essence, our approach involves iteratively updating the restoring force on big (small) particles. So the mth update of the restoring force has the following form:

$$F_{res,b/s}^{\text{IM,m}}(y) = F_{res,b/s}^{\text{IM,m}-1}(y) + \Delta F_{res,b/s}^{\text{m}}(y) \tag{4.1}$$

The iterative correction to the spatially varying restoring force, denoted as $\Delta F_{\text{res},b/s}^{\text{m}}(y)$, is determined using the following equation:

$$\Delta F_{b/s}^{\text{m}}(y) = -\frac{\kappa P_0 N \langle d \rangle^2}{N_{b/s}} \frac{\partial \left(\psi_{b/s}^{\text{m}-1}(y) - \psi_{b/s}^{\text{C}}(y) \right)}{\partial y} \tag{4.2}$$

where $\psi_{b/s}^{\text{x}}(y) = \frac{\phi_{b/s}^{\text{x}}(y)}{\phi_{\text{tot}}(y)}$ represents the relative packing fractions, defined in terms of the individual species packing fractions $\phi_{s/b}$ and the total ϕ_{tot}. Additionally, $F_{b/s}^{\text{IM},0}(y) = 0$.

The superscript $(m-1)$ denotes the profile after a stationary flow is reached while applying the $F^{(m-1)}$ force. The superscript C signifies the Couette case, in the absence of gravitational forces. κ is a dimensionless prefactor set to 0.2. The iterative restoring forces also satisfy force balance, $F_{res,b}^{\text{IM}}(y)N_b + F_{res,s}^{\text{IM}}(y)N_s = 0$.

The iterative process of adjusting restoring forces for both large and small particles continues until the packing fraction profiles resemble those of the fully homogenized pure Couette flow, falling within the limits defined by our noise level.

4.2.3   Constant Gravity

For both frictionless and frictional mixtures, an increasing tilt in the total and relative packing fraction profiles is observed with rising gravity, for all the investigated rescaled constant gravities $g^* = \pi \rho \langle d \rangle |g|/(4P_0)$ under constant global shear rates, as depicted in Figs. 4.5($\mathbf{a}$, $\mathbf{e}$, $\mathbf{i}$) and 4.6($\mathbf{a}$, $\mathbf{d}$, $\mathbf{g}$), respectively, in comparison to the corresponding Couette cases. This inclination is anticipated since we now have a spatially varying inertial number profile due to the spatially varying pressure. However, the segregation,

quantified by ψ_b, cannot be solely attributed to the varying inertial number. This is evident from the fact that the local rheology remains constant with composition. Instead, segregation is driven by segregation forces induced by the spatially varying pressure and shear-rate profiles.

In all cases, an initial boundary effect related to particle type is observed, leading to an accumulation of small particles at the boundaries. This is indicated by a sharp decrease in ψ_b at the boundaries, where small particles better fill the gaps of the rough walls. This boundary effect persists even in the presence of gravity, as will be further demonstrated when restoring forces are applied.

We now apply two restoring forces, the Harmonic Method (HM) and the Iterative Method (IM), and observe their successful counteraction of segregation. This is evident in Figs. 4.5($\mathbf{b}, \mathbf{c}, \mathbf{f}, \mathbf{g}, \mathbf{j}, \mathbf{k}$) and 4.6($\mathbf{b}, \mathbf{e}, \mathbf{h}$), where $\psi_b - \psi_b^C$ is close to zero (within noise), indicating the same relative packing fraction profile as the corresponding Couette cases. In the frictionless case, the ϕ profile remains essentially the same, while a small shift to higher total packing fractions is observed when applying the restoring forces. Both methods yield the same profile. Although force profiles differ slightly—HM being flat and IM showing slight slopes—the differences are within our noise level and hence the two methods give equivalent forces and show that $F_{\mathrm{res}} \sim |g|$, as reported by [68].

A more detailed examination shows that applying a restoring force homogenizes the flowing mixture while maintaining a constant μ profile. Other profiles, such as I, ϕ, $\omega/\dot{\gamma}$, and Z, exhibit only slight alterations when the force is applied (see more details in paper II). However, the granular temperature Θ_{yy} shows a significant decrease after applying a restoring force, particularly in the high-pressure region. The perturbation in the properties is more substantial for frictional mixtures than for frictionless ones and increases with increasing gravity (see Fig. 4.7).

4.2.4   Linearly increasing gravity

In the scenario with linearly increasing gravity starting from zero at the top wall, represented by its rescaled maximum value at the bottom of the cell, $g_{\mathrm{max}}^* = \pi\rho\langle d\rangle|g|_{\mathrm{max}}/(4P_0)$, our iterative method which allows for spatial variation of the calculated forces works to find the restoring force profiles both for the frictionless and frictional mixtures as shown in Fig. 4.8, while the harmonic method is naturally inadequate to find the required restoring force since the harmonic method, by definition gives a constant restoring force profile and con not take account for spatial variation of the force. The magnitude of the restoring forces found by IM is linearly increasing from the top,

mirroring the gravity, i.e., $F_{\text{res}} \sim |g|$. To validate this, we apply a Test force that linearly increases with gravity and has the max magnitude determined from the constant gravity simulations. These Test forces also successfully homogenize the samples (see Fig. 4.8), confirming that the restoring forces and, consequently, segregation forces are solely functions of the local gravity, with no detectable influence from its gradient.

A more in-depth analysis reveals that similar to the case of constant gravity, the application of a restoring force homogenizes the flowing mixture while maintaining a constant μ profile. Other profiles, such as I, ϕ, $\omega/\dot{\gamma}$, and Z, experience only slight alterations when the force is applied. However, the granular temperature Θ_{yy} undergoes a significant decrease after the application of a restoring force, particularly in the high-pressure region. Again, the perturbation in the properties is more substantial for frictional mixtures than for frictionless ones and increases with escalating gravity (see appendix of paper II). Further investigation into the changes in granular temperature following the application of restoring forces may provide insights into the reasons for segregation, potentially linking it to altered fluctuations in the flowing mixture.
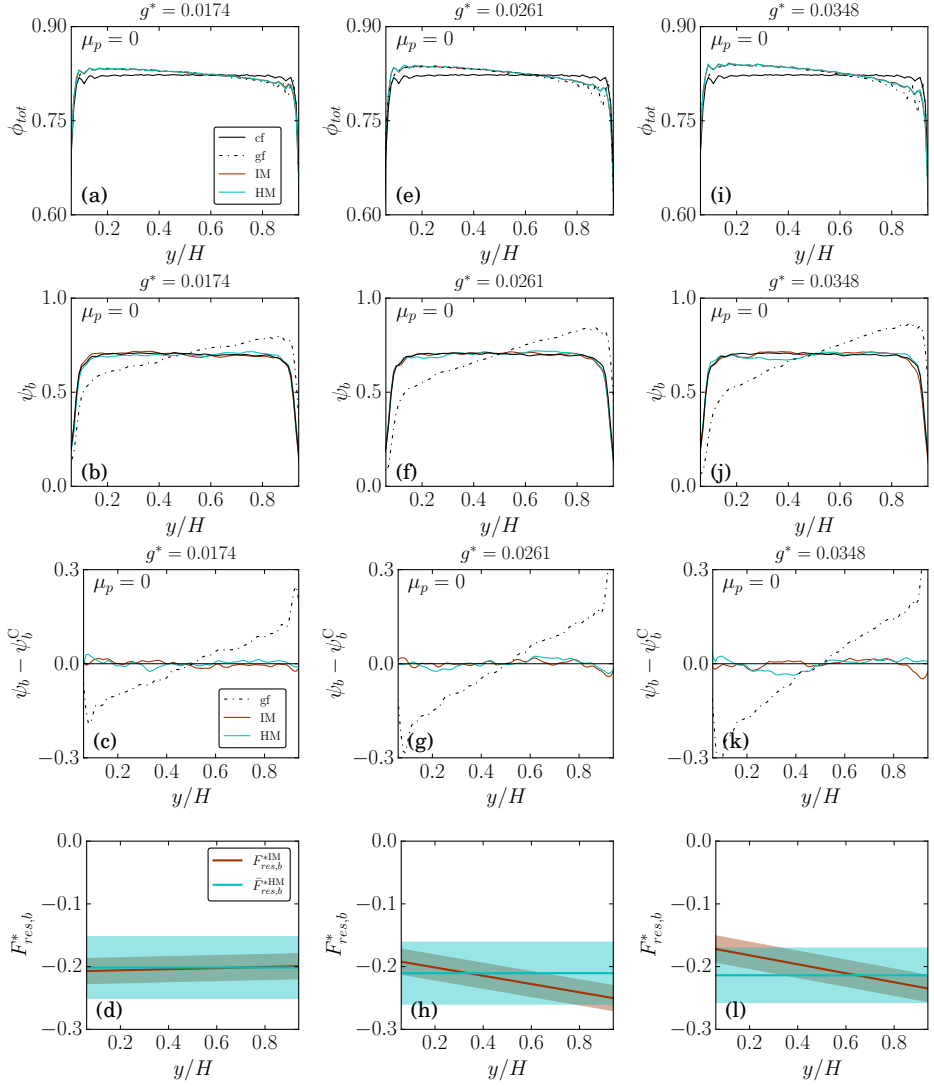
Figure 4.5: The upper panel ((**a**), (**e**), and (**i**)) depicts profiles of the total packing fraction, ϕ_{tot}, for frictionless ($\mu_p = 0$) mixtures in different scenarios: Couette flow (cf), gravity flow (gf) without restoring forces, and after applying the Iterative Method (IM) and the Harmonic Method (HM) forces at various constant gravities g^*. The second and third rows from the top ((**b**), (**f**), and (**j**)) and ((**c**), (**g**), and (**k**)) illustrate the corresponding profiles of ψ_b and $\psi_b - \psi_b^C$, respectively. In the bottom row ((**d**), (**h**), and (**l**)), the normalized restoring forces on the large discs, $F_{\text{res,b}}^*$, are plotted. The shaded regions indicate either the standard deviation (HM) or the estimated error (IM) of the calculated forces.
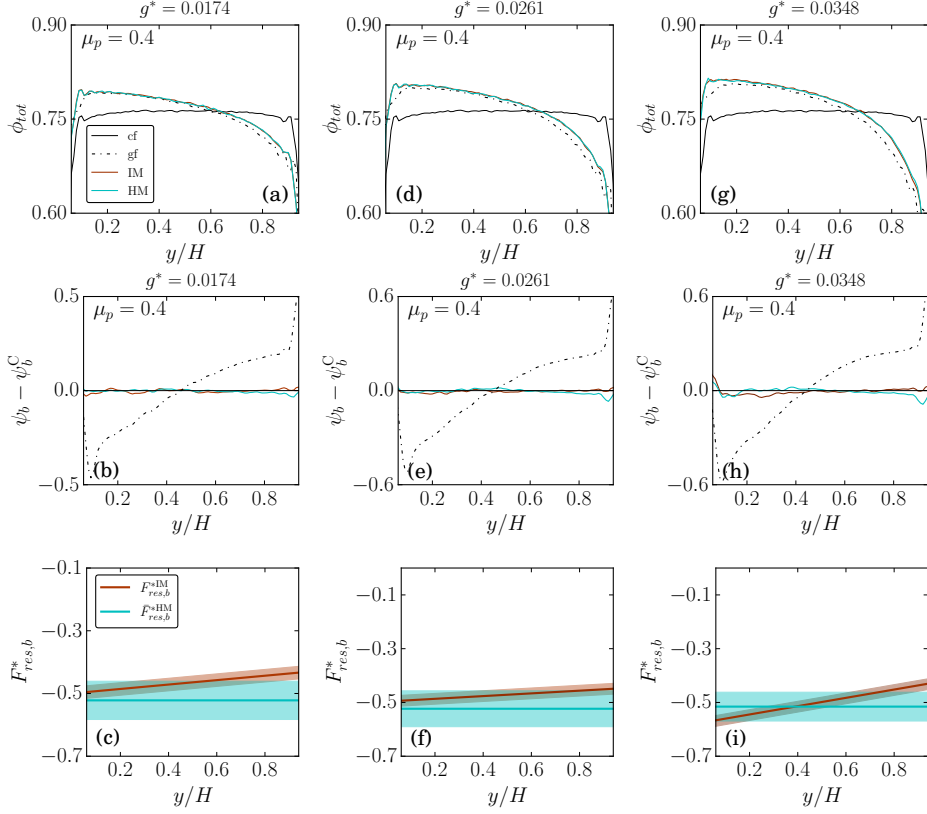
Figure 4.6: The upper panel ((**a**), (**d**), and (**g**)) displays profiles of the total packing fraction, ϕ_{tot}, for frictional ($\mu_p = 0.4$) mixtures in different scenarios: Couette flow (cf), gravity flow (gf) without restoring forces, and after applying the Iterative Method (IM) and the Harmonic Method (HM) forces at various constant gravities g^*. The middle row ((**b**), (**e**), and (**h**)) illustrates the corresponding profiles of $\psi_b - \psi_b^C$. In the bottom row ((**c**), (**f**), and (**i**)), the normalized restoring forces on the large discs, $F_{\text{res},b}^*$, are plotted. The shaded regions indicate the standard deviation (HM) or estimated error (IM) of the calculated forces.
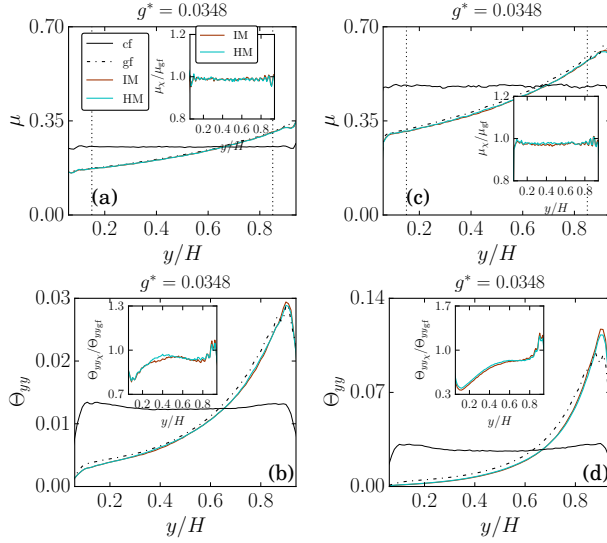
Figure 4.7: Profiles of (**a**) and (**c**) depict the friction coefficient μ for frictionless ($\mu_p = 0$) and frictional ($\mu_p = 0.4$) mixtures, respectively at $g^* = 0.0348$. (**b**), (**d**), present the rescaled granular temperature Θ_{yy} for frictionless ($\mu_p = 0$) and frictional ($\mu_p = 0.4$) mixtures, respectively at the same constant gravity field. The profiles are illustrated in the Couette flow (solid black curves), gravity flow gf (dashed-dotted black curves), after applying the final iterative method IM restoring force (brown curves), and after applying the harmonic method HM restoring force (cyan curves). The insets in the figures show the ratio between each of the parameters profiles, μ_χ/μ_{gf} and $\Theta_{yy\,\chi}/\Theta_{yy\,\text{gf}}$ when applying restoring forces to without restoring forces, *i.e.* gravity flow, where χ is either (IM) (brown curves) or (HM) (cyan curves). The dotted vertical lines in the I and μ profiles indicate where the profiles are cut for use in the μ-vs-I.
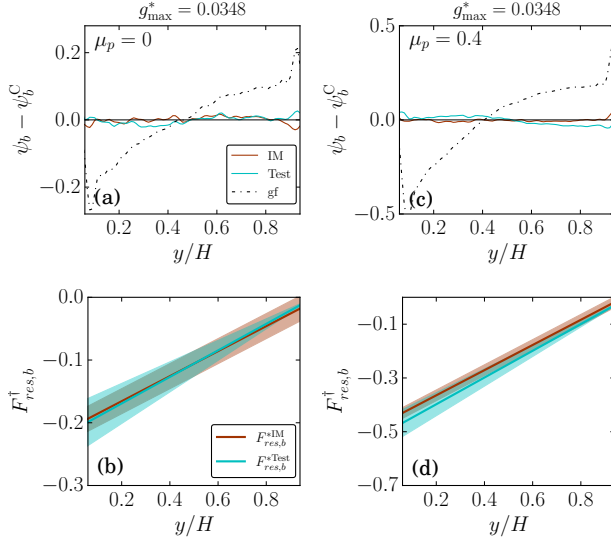
Figure 4.8: Profiles of $\psi_b - \psi_b^C$ in (**a**) and (**c**) for frictionless ($\mu_p = 0$) and frictional ($\mu_p = 0.4$) mixtures, respectively at $g_{\max}^* = 0.0348$ after applying the final IM, the Test force and in the gravity flow without any restoring forces (gf). In (**b**) and (**d**), the respective normalized restoring forces on the large discs in frictionless ($\mu_p = 0$) and frictional ($\mu_p = 0.4$) mixtures denoted as $F_{res,b}^\dagger$, are presented. The shaded regions indicate the estimate of standard error in the calculated forces.

References

[1] Maurice Kleman and Oleg D Laverntovich. *Soft matter physics: an introduction*. Springer Science & Business Media, 2007.

[2] Hsiao-Chuan Liu, Piotr Kijanka, and Matthew W Urban. Acoustic radiation force optical coherence elastography for evaluating mechanical properties of soft condensed matters and its biological applications. *Journal of Biophotonics*, 13(3): e201960134, 2020.

[3] Jonathan J Stickel and Robert L Powell. Fluid mechanics and rheology of dense suspensions. *Annu. Rev. Fluid Mech.*, 37:129–149, 2005.

[4] Bruno Andreotti, Yoël Forterre, and Olivier Pouliquen. *Granular media: between fluid and solid*. Cambridge University Press, 2013.

[5] Martin Trulsson. Rheology and shear jamming of frictional ellipses. *Journal of Fluid Mechanics*, 849:718–740, 2018.

[6] JA Todd. L. fejes toth, regular figures (pergamon press, 1964), xi+ 339 pp., 84s. *Proceedings of the Edinburgh Mathematical Society*, 14(2):174–175, 1964.

[7] Aleksandar Donev, Frank H Stillinger, PM Chaikin, and Salvatore Torquato. Unusually dense crystal packings of ellipsoids. *Physical review letters*, 92(25): 255506, 2004.

[8] G Delaney, D Weaire, Stefan Hutzler*, and S Murphy. Random packing of elliptical disks. *Philosophical Magazine Letters*, 85(2):89–96, 2005.

[9] Romain Guises, Jiansheng Xiang, John-Paul Latham, and Antonio Munjiza. Granular packing: numerical simulation and the characterisation of the effect of particle shape. *Granular Matter*, 11(5):281–292, 2009.

[10] Aleksandar Donev, Ibrahim Cisse, David Sachs, Evan A Variano, Frank H Stillinger, Robert Connelly, Salvatore Torquato, and Paul M Chaikin. Improving

the density of jammed disordered packings using ellipsoids. *Science*, 303(5660): 990–993, 2004.

[11] Weining Man, Aleksandar Donev, Frank H Stillinger, Matthew T Sullivan, William B Russel, David Heeger, Souheil Inati, Salvatore Torquato, and PM Chaikin. Experiments on random packings of ellipsoids. *Physical review letters*, 94(19):198001, 2005.

[12] Leonardo E Silbert. Jamming of frictional spheres and random loose packing. *Soft Matter*, 6(13):2918–2924, 2010.

[13] Lateef Temitope Akanji. Simulation of pore-scale flow using finite element-methods. 2010.

[14] Robert P Behringer and Bulbul Chakraborty. The physics of jamming for granular materials: a review. *Reports on Progress in Physics*, 82(1):012601, 2018.

[15] Pierre-Emmanuel Peyneau and Jean-Noël Roux. Frictionless bead packs have macroscopic friction, but no dilatancy. *Physical review E*, 78(1):011307, 2008.

[16] Émilien Azéma, Farhang Radjai, and Jean-Noël Roux. Internal friction and absence of dilatancy of packings of frictionless polygons. *Physical Review E*, 91 (1):010202, 2015.

[17] Varghese Babu, Deng Pan, Yuliang Jin, Bulbul Chakraborty, and Srikanth Sastry. Dilatancy, shear jamming, and a generalized jamming phase diagram of frictionless sphere packings. *Soft Matter*, 17(11):3121–3127, 2021.

[18] Andrea J Liu and Sidney R Nagel. The jamming transition and the marginally jammed solid. *Annu. Rev. Condens. Matter Phys.*, 1(1):347–369, 2010.

[19] Heinrich M Jaeger, Sidney R Nagel, and Robert P Behringer. The physics of granular materials. *Physics today*, 49(4):32–39, 1996.

[20] Liuchi Li, Eloïse Marteau, and José E Andrade. Capturing the inter-particle force distribution in granular material using ls-dem. *Granular Matter*, 21(3): 1–16, 2019.

[21] Emilien Azéma and Farhang Radjai. Force chains and contact network topology in sheared packings of elongated particles. *Physical review E*, 85(3):031303, 2012.

[22] Emilien Azéma and Farhang Radjaï. Stress-strain behavior and geometrical properties of packings of elongated particles. *Physical Review E*, 81(5):051304, 2010.

[23] Farhang Radjai, Dietrich E Wolf, Michel Jean, and Jean-Jacques Moreau. Bimodal character of stress transmission in granular packings. *Physical review letters*, 80(1):61, 1998.

[24] Farhang Radjai, J-Y Delenne, Emilien Azéma, and Stéphane Roux. Fabric evolution and accessible geometrical states in granular materials. *Granular Matter*, 14(2):259–264, 2012.

[25] François Boyer, Élisabeth Guazzelli, and Olivier Pouliquen. Unifying suspension and granular rheology. *Physical review letters*, 107(18):188301, 2011.

[26] Pierre Jop, Yoël Forterre, and Olivier Pouliquen. A constitutive law for dense granular flows. *Nature*, 441(7094):727–730, 2006.

[27] Ralph Alger Bagnold. Experiments on a gravity-free dispersion of large solid spheres in a newtonian fluid under shear. *Proceedings of the Royal Society of London. Series A. Mathematical and Physical Sciences*, 225(1160):49–63, 1954.

[28] Edward M Purcell. Life at low reynolds number. *American journal of physics*, 45 (1):3–11, 1977.

[29] John Happel and Howard Brenner. *Low Reynolds number hydrodynamics: with special applications to particulate media*, volume 1. Springer Science & Business Media, 2012.

[30] Elisabeth Guazzelli and Jeffrey F Morris. *A physical introduction to suspension dynamics*, volume 45. Cambridge University Press, 2011.

[31] Allen T Chwang and T Wu. Hydromechanics of low-reynolds-number flow. part 2. singularity method for stokes flows. *Journal of Fluid mechanics*, 67(4): 787–815, 1975.

[32] Sunil Datta and Deepak Kumar Srivastava. Stokes drag on axially symmetric bodies: a new approach. In *Proceedings of the Indian Academy of Sciences-Mathematical Sciences*, volume 109, pages 441–452. Springer, 1999.

[33] Albert Einstein. Berichtigung zu meiner arbeit: Eine neue bestimmung der moleküldimensionen. *Annalen der Physik*, 339(3):591–592, 1911.

[34] Élisabeth Guazzelli and Olivier Pouliquen. Rheology of dense granular suspensions. *Journal of Fluid Mechanics*, 852, 2018.

[35] Daisuke Ishima and Hisao Hayakawa. Scaling laws for frictional granular materials confined by constant pressure under oscillatory shear. *Physical Review E*, 101(4):042902, 2020.

[36] Kyu Hyun, Manfred Wilhelm, Christopher O Klein, Kwang Soo Cho, Jung Gun Nam, Kyung Hyun Ahn, Seung Jong Lee, Randy H Ewoldt, and Gareth H McKinley. A review of nonlinear oscillatory shear tests: Analysis and application of large amplitude oscillatory shear (laos). *Progress in Polymer Science*, 36(12): 1697–1753, 2011.

[37] Ronald G Larson. *The structure and rheology of complex fluids*, volume 150.

[38] Junhao Dong and Martin Trulsson. Transition from steady shear to oscillatory shear rheology of dense suspensions. *Physical Review E*, 102(5):052605, 2020.

[39] Frédéric Blanc, François Peters, and Elisabeth Lemaire. Local transient rheological behavior of concentrated suspensions. *Journal of Rheology*, 55(4):835–854, 2011.

[40] François Peters, Giovanni Ghigliotti, Stany Gallier, Frédéric Blanc, Elisabeth Lemaire, and Laurent Lobry. Rheology of non-brownian suspensions of rough frictional particles under shear reversal: A numerical study. *Journal of rheology*, 60(4):715–732, 2016.

[41] Christopher Ness and Jin Sun. Two-scale evolution during shear reversal in dense suspensions. *Physical Review E*, 93(1):012604, 2016.

[42] Neil YC Lin, Christopher Ness, Michael E Cates, Jin Sun, and Itai Cohen. Tunable shear thickening in suspensions. *Proceedings of the National Academy of Sciences*, 113(39):10774–10778, 2016.

[43] Christopher Ness, Zhongyang Xing, and Erika Eiser. Oscillatory rheology of dense, athermal suspensions of nearly hard spheres below the jamming point. *Soft Matter*, 13(19):3664–3674, 2017.

[44] Christopher Ness, Romain Mari, and Michael E Cates. Shaken and stirred: Random organization reduces viscosity and dissipation in granular suspensions. *Science advances*, 4(3):eaar3296, 2018.

[45] David J Pine, Jerry P Gollub, John F Brady, and Alexander M Leshansky. Chaos and threshold for irreversibility in sheared suspensions. *Nature*, 438(7070):997–1000, 2005.

[46] Laurent Corte, Paul M Chaikin, Jerry P Gollub, and David J Pine. Random organization in periodically driven systems. *Nature Physics*, 4(5):420–424, 2008.

[47] Laurent Corté, Sharon J Gerbode, Weining Man, and David J Pine. Self-organized criticality in sheared suspensions. *Physical review letters*, 103(24): 248301, 2009.

[48] Lihi Shachar-Berman, Yan Ostrovski, Alessandro De Rosis, Stavros Kassinos, and Josué Sznitman. Transport of ellipsoid fibers in oscillatory shear flows: Implications for aerosol deposition in deep airways. *European Journal of Pharmaceutical Sciences*, 113:145–151, 2018.

[49] J Férec, MC Heuzey, Gilles Ausias, and PJ Carreau. Rheological behavior of fiber-filled polymers under large amplitude oscillatory shear flow. *Journal of non-newtonian fluid mechanics*, 151(1-3):89–100, 2008.

[50] F-X Riguidel, A Hansen, and D Bideau. Gravity-driven motion of a particle on an inclined plane with controlled roughness. *EPL (Europhysics Letters)*, 28(1):13, 1994.

[51] Mohammadreza Alizadeh, Ali Hassanpour, Mehrdad Pasha, Mojtaba Ghadiri, and Andrew Bayly. The effect of particle shape on predicted segregation in binary powder mixtures. *Powder Technology*, 319:313–322, 2017.

[52] A Shimosaka, Iyo Nousou, Yoshiyuki Shirakawa, and Jusuke Hidaka. Effect of particle shape on size segregation of particles. *Chemical Engineering Transactions*, 32:2143–2148, 2013.

[53] Atsuko Shimosaka, Yoshiyuki Shirakawa, and Jusuke Hidaka. Effects of particle shape and size distribution on size segregation of particles. *Journal of chemical engineering of Japan*, page 12we179, 2012.

[54] JM Ottino and DV Khakhar. Mixing and segregation of granular materials. *Annual review of fluid mechanics*, 32(1):55–91, 2000.

[55] P Tang and VM Puri. Methods for minimizing segregation: a review. *Particulate Science and Technology*, 22(4):321–337, 2004.

[56] Rémi Jullien and Paul Meakin. A mechanism for particle size segregation in three dimensions. *Nature*, 344(6265):425–427, 1990.

[57] Gerard Viner Middleton. Experimental studies related to flysch sedimentation. *Flysch sedimentolgy in North America*, 7:253–272, 1970.

[58] SB Savage and CKK Lun. Particle size segregation in inclined chute flow of dry cohesionless granular solids. *Journal of fluid mechanics*, 189:311–335, 1988.

[59] Andrew M Scott and John Bridgwater. Interparticle percolation: a fundamental solids mixing mechanism. *Industrial & Engineering Chemistry Fundamentals*, 14 (1):22–27, 1975.

[60] EE Ehrichs, HM Jaeger, Greg S Karczmar, James B Knight, Vadim Yu Kuperman, and Sidney R Nagel. Granular convection observed by magnetic resonance imaging. *Science*, 267(5204):1632–1634, 1995.

[61] Anthony Rosato, Katherine J Strandburg, Friedrich Prinz, and Robert H Swendsen. Why the brazil nuts are on top: Size segregation of particulate matter by shaking. *Physical review letters*, 58(10):1038, 1987.

[62] J Duran, J Rajchenbach, and E Clément. Arching effect model for particle size segregation. *Physical review letters*, 70(16):2431, 1993.

[63] James B Knight, Heinrich M Jaeger, and Sidney R Nagel. Vibration-induced size separation in granular media: The convection connection. *Physical review letters*, 70(24):3728, 1993.

[64] John Mark Nicholas Timm Gray. Particle segregation in dense granular flows. *Annual review of fluid mechanics*, 50:407–433, 2018.

[65] Paul B Umbanhowar, Richard M Lueptow, and Julio M Ottino. Modeling segregation in granular flows. *Annual review of chemical and biomolecular engineering*, 10:129–153, 2019.

[66] Anthony Thornton. A brief review of (multi-scale) modelling approaches to segregation. In *EPJ Web of Conferences*, volume 249, page 01004. EDP Sciences, 2021.

[67] Anurag Tripathi and DV Khakhar. Numerical simulation of the sedimentation of a sphere in a sheared granular fluid: a granular stokes experiment. *Physical review letters*, 107(10):108001, 2011.

[68] François Guillard, Yoël Forterre, and Olivier Pouliquen. Scaling laws for segregation forces in dense sheared granular flows. *Journal of Fluid Mechanics*, 807, 2016.

[69] Lu Jing, Julio M Ottino, Richard M Lueptow, and Paul B Umbanhowar. A unified description of gravity-and kinematics-induced segregation forces in dense granular flows. *arXiv preprint arXiv:2103.09386*, 2021.

[70] CJ Coetzee. Calibration of the discrete element method. *Powder Technology*, 310:104–142, 2017.

[71] Lawrence K Nordell. Particle flow modelling: Transfer chutes and other applications. In *International Materials Handling Conference (BELTCON 9), Johannesburg, South Africa*, 1997.

[72] David B Hastie, Andrew P Grima, and Peter W Wypych. Validation of particle flow through a conveyor transfer hood via particle velocity analysis. 2008.

[73] Torsten Gröger and André Katterfeld. On the numerical calibration of discrete element models for the simulation of bulk solids. In *Computer Aided Chemical Engineering*, volume 21, pages 533–538. Elsevier, 2006.

[74] Matthew D Sinnott and Paul W Cleary. The effect of particle shape on mixing in a high shear mixer. *Computational Particle Mechanics*, 3(4):477–504, 2016.

[75] Eutiquio Gallego, Angel Ruiz, and Pedro J Aguado. Simulation of silo filling and discharge using ansys and comparison with experimental data. *Computers and Electronics in Agriculture*, 118:281–289, 2015.

[76] CJ Coetzee. Discrete and continuum modelling of soil cutting. *Computational Particle Mechanics*, 1(4):409–423, 2014.

[77] Frédéric Da Cruz, Sacha Emam, Michaël Prochnow, Jean-Noël Roux, and François Chevoir. Rheophysics of dense granular materials: Discrete simulation of plane shear flows. *Physical Review E*, 72(2):021309, 2005.

[78] MJ Neale and DD Fuller. Theory and practice of lubrication for engineers, 1984.

[79] Wenbin Zhang, Reiji Noda, and Masayuki Horio. Evaluation of lubrication force on colliding particles for dem simulation of fluidized beds. *Powder Technology*, 158(1-3):92–101, 2005.

[80] RG Cox. The motion of suspended particles almost in contact. *International Journal of Multiphase Flow*, 1(2):343–371, 1974.

[81] Martin Trulsson, Bruno Andreotti, and Philippe Claudin. Transition from the viscous to inertial regime in dense suspensions. *Physical review letters*, 109(11):118305, 2012.

[82] Pierre Grégoire Rognon, Itai Einav, and Cyprien Gay. Flowing resistance and dilatancy of dense suspensions: lubrication and repulsion. *Journal of Fluid Mechanics*, 689:75–96, 2011.

[83] Daan Frenkel and Berend Smit. *Understanding molecular simulation: from algorithms to applications*, volume 1. Elsevier, 2001.

[84] M Trulsson, E DeGiuli, and M Wyart. Effect of friction on dense suspension flows of hard particles. *Physical Review E*, 95(1):012605, 2017.

[85] F. Alonso-Marroquín and H. J. Herrmann. Ratcheting of granular materials. *Phys. Rev. Lett.*, 92:054301, Feb 2004. doi: 10.1103/PhysRevLett.92.054301. URL `https://link.aps.org/doi/10.1103/PhysRevLett.92.054301`.

[86] Junhao Dong and Martin Trulsson. Oscillatory shear flows of dense suspensions at imposed pressure: Rheology and micro-structure. *arXiv preprint arXiv:2011.13215*, 2020.

[87] Yifei Duan, Lu Jing, Paul B Umbanhowar, Julio M Ottino, and Richard M Lueptow. Segregation forces in dense granular flows: closing the gap between single intruders and mixtures. *Journal of Fluid Mechanics*, 935, 2022.

Scientific publications

Author contributions

Paper I: Orientational arrest in dense suspensions of elliptical particles under oscillatory shear flows

I executed simulations, analyzed the results using my own analysis script, and contributed to writing the majority of the manuscript.

Paper II: An iterative method for measuring spatial segregation forces in bidisperse granular flow mixtures under various gravity fields

I participated in developing the code and the theory. I executed the simulations and analyzed the results with my scripts. I wrote most parts of the manuscript.

Faculty of Science
Department of Chemistry
Division of Computational Chemistry

9 789174 229646